โครงสร้างผลึกของคอปเปอร์อินเดียมไดซิลินายด์ภายใต้ความดันสูง

นางสาว วราลักษณ์ แสงสุวรรณ

วิทยานิพนธ์นี้เป็นส่วนหนึ่งของการศึกษาตามหลักสูตรปริญญาวิทยาศาสตรมหาบัณฑิต
สาขาวิชาฟิสิกส์ ภาควิชาฟิสิกส์
คณะวิทยาศาสตร์ จุฬาลงกรณ์มหาวิทยาลัย
ปีการศึกษา 2547

ISBN 974-17-6589-4

CRYSTAL STRUCTURE OF $CuInSe_2$ UNDER HIGH PRESSURE

Miss Varalak Saengsuwan

A Thesis Submitted in Partial Fulfillment of the Requirements
for the Degree of Master of Science in Physics
Department of Physics
Faculty of Science
Chulalongkorn University
Academic Year 2004
ISBN 974-17-6589-4

Thesis Title	Crystal Structure of $CuInSe_2$ under High Pressure
By	Miss Varalak Saengsuwan
Field of study	Physics
Thesis Advisor	Dr. Thiti Bovornratanaraks

Accepted by the Faculty of Science, Chulalongkorn University in Partial Fulfillment of the Requirements for the Master’s Degree

……………………………………………….. Dean of the Faculty of Science
(Professor Piamsak Menasveta, Ph. D.)

THESIS COMMITTEE

……………………………………………….. Chairman
(Assistant Professor Kajornyod Yoodee, Ph. D.)

……………………………………………….. Thesis Advisor
(Thiti Bovornratanaraks, Ph. D.)

……………………………………………….. Member
(Assistant Professor Sukkaneste Tungasmita, Ph. D.)

……………………………………………….. Member
(Jessada Sukpitak, Ph. D.)

นางสาว วราลักษณ์ แสงสุวรรณ: โครงสร้างผลึกของคอปเปอร์อินเดียมไดซิลินายด์ภายใต้ความดันสูง (CRYSTAL STRUCTURE OF $CuInSe_2$ UNDER HIGH PRESSURE) อ. ที่ปรึกษา: ดร. ธิติ บวรรัตนารักษ์, 69 หน้า. ISBN 974-17-6589-4.

คอปเปอร์อินเดียมไดซิลินายด์ ($CuInSe_2$) คือสารกึ่งตัวนำ (Semiconductor) ซึ่งทำหน้าที่เป็นตัวดูดกลืนพลังงานโฟตอนภายในเซลล์สุริยะ และยังสามารถนำไปใช้ในการทดลองเชิงแสงได้อย่างมีประสิทธิภาพ ทำให้ในปัจจุบันมีการศึกษาสมบัติของคอปเปอร์อินเดียมไดซิลินายด์ในสภาวะแวดล้อมต่างๆ มากขึ้น ซึ่งสมบัติของสารต่างๆ ทั้งทางเคมี และทางฟิสิกส์จะเปลี่ยนแปลงไปตามโครงสร้างผลึกที่ขึ้นกับอุณหภูมิ และความดันของสิ่งแวดล้อม โดยในวิทยานิพนธ์นี้ได้ทำการศึกษาโครงสร้างผลึกของคอปเปอร์อินเดียมไดซิลินายด์ในสภาวะที่ความดันของสิ่งแวดล้อมสูงขึ้น ที่ผ่านมาในปี ค.ศ.1996 T.Tinoco และทีมงาน ได้ทำการศึกษาโครงสร้างของคอปเปอร์อินเดียมไดซิลินายด์ในระดับความดันสูงสุด 290 กิโลบาร์ โดยใช้การเลี้ยวเบนของรังสีเอ็กซ์ชนิดกระจายพลังงาน (Energy Dispersive X-rays Diffraction) แบบผง ซึ่งใช้รังสีเอ็กซ์ที่มาจากแหล่งกำเนิดรังสีซินโครตรอน (Synchrotron Radiation Source) ในการหาโครงสร้าง และใช้ DAC แบบ Merill-Bassett Cell ในการเพิ่มความดัน แต่ในงานวิจัยนี้เพื่อให้ได้ข้อมูลที่มีความละเอียดมากยิ่งขึ้น จึงได้ทำการเก็บข้อมูลทางการเลี้ยวเบนของรังสีเอ็กซ์ชนิดกระจายมุม (Angle Dispersive X-rays Diffraction) แบบผงด้วยเครื่องมือ Image-Plate และใช้รังสีเอ็กซ์ความยาวคลื่น 0.4654 Å ที่มาจากแหล่งกำเนิดรังสีซินโครตรอนในการหาโครงสร้างผลึกของคอปเปอร์อินเดียมไดซิลินายด์ ส่วนการเพิ่มความดันให้กับสารนั้น เราได้ใช้ DAC แบบ DXR-6 Diamond anvil cell โดยความดันสูงสุดที่ทำการทดลองจะอยู่ที่ประมาณ 532 กิโลบาร์ ซึ่งเป็นระดับความดันที่ยังไม่เคยมีการศึกษามาก่อน

ภาควิชา ฟิสิกส์ ลายมือชื่อนิสิต...
สาขาวิชา ฟิสิกส์ ลายมือชื่ออาจารย์ที่ปรึกษา......................................
ปีการศึกษา 2547

4572480023: MAJOR PHYSICS
KEY WORD: X-RAY POWDER DIFFRACTION / IMAGE-PLATE / DAC / $CuInSe_2$ / HIGH PRESSURE

VARALAK SAENGSUWAN: CRYSTAL STRUCTURE OF $CuInSe_2$ UNDER HIGH PRESSURE. THESIS ADVISOR: DR. THITI BOVORNRATANARAKS, 69 pp. ISBN 974-17-6589-4.

The $CuInSe_2$ has recently emerged as a very promising material for photovoltaic solar-energy application, due partially to the fact that it is probably the strongest absorbing semiconductor under sunlight. Furthermore, $CuInSe_2$ is also widely used in optical laboratories. Since the chemical and physical properties of materials are governed by the temperature and pressure. The crystal structure of this material is studied under various thermodynamic conditions. Because of the advancement in technology, the structure studies of this material under high pressure are interested for various fields of work.

In 1996, the crystal structure of $CuInSe_2$ and their structural phase transitions under high pressure were investigated by T.Tinoco *et al*. They studied the crystal structure of $CuInSe_2$ under the maximum pressure of 290 kbar by using energy dispersive x-rays diffraction with synchrotron radiation and Merill-Bassett diamond anvil cell. In this research, the Angle Dispersive X-rays Powder Diffraction is used with Image-Plate method and x-rays with $\lambda = 0.4654$ Å on station 9.1 at Synchrotron Radiation Source, Daresbury, UK for high quality data. DXR-6 Diamond anvil cell is used for generating pressure up to 532 kbar which the structural studies of this material at this pressure have never been done before. Ruby fluorescence technique is used for pressure calibration.

Department of Physics	Student’s signature...................................
Field of study Physics	Advisor’s signature...................................
Academic year 2004	

Acknowledgments

The author gratefully acknowledge the support of all who have, directly or indirectly, contributed to this thesis.

First, my great appreciation express to Dr. Thiti Bovornratanaraks , my thesis advisor, for his attention, encouragement, considerate guidance and useful comments to make this thesis accomplish. Besides, I also thank him for giving me a great opportunity to participate in ICTP School on Synchrotron Radiation and Applications at Trieste, Italy.

I wish to express my sincere appreciation to Assist. Prof. Kajornyod Yoodee, Ph.D. for his considerate guidance and great helpful comments. My appreciation also extend to the committee for inspecting, and checking on my work very carefully.

My great gratitude express to Dr. M.I. McMahon, Daresbury Laboratory, UK for his technical assistance in preparing the Angle dispersive X-rays powder diffraction data of $CuInSe_2$ under high-pressure by using Synchrotron Radiation.

I wish to express my sincere appreciation to Department of Physics and Graduate School, Chulalongkorn University for their financial supports

My special thanks also to my friends at Sainumpeung School, Mahidol University and Chulalongkorn University for their help and sincere friendship.

Finally, I wish to express my sincere gratitude to my parents and my sister for their love, support and encouragement to make me succeed.

Table of Contents

List of Tables

List of Figures

Figure Page

CHAPTER I

Introduction

The ternary-compound IB-IIIA-VIA$_2$ chalcopyrite semiconductors (e.g. CuGaSe$_2$) form a large group of semiconducting materials with various optical, electrical and structural properties. One of them, CuInSe$_2$ (Copper Indium Diselenide) has received considerable attention recently because of its potential in photovoltaic solar-energy application. Figure 1 shows the absorption spectrum of CuInSe$_2$ complied by Jaffe *et al.* [1]. The absorption of this material is stronger than those of other photovoltaic semiconductors. In the case of Cu-III-VI$_2$, their direct energy gaps (E$_g$) increase with the increasing pressure similar to those of the II-IV binary compounds [2]. Nevertheless, the relative magnitude of $\frac{dE_g}{dP}$ in

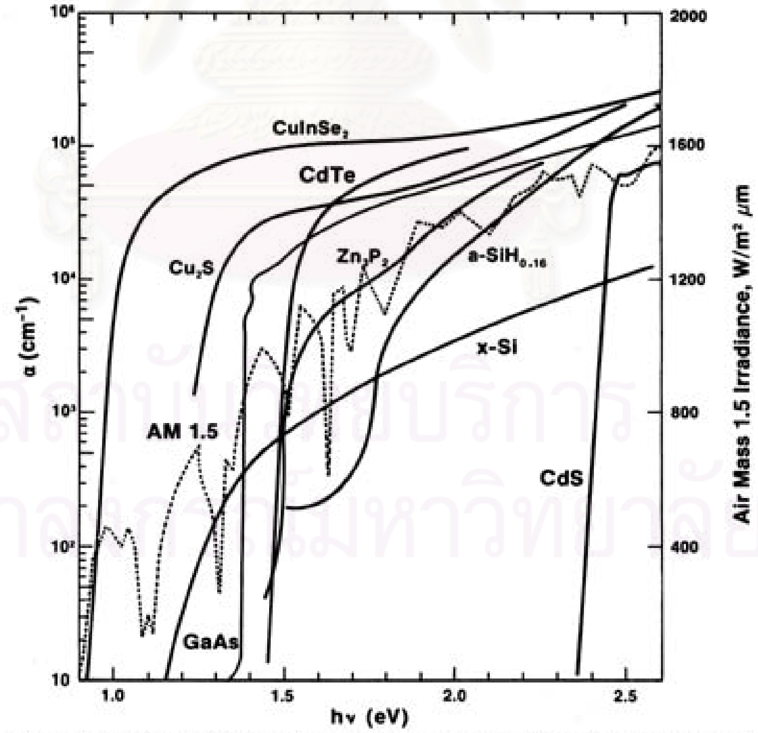

Figure 1: Absorption Spectrum of CuInSe$_2$ compared with that other photovoltaic semiconductors. For comparison, Jaffe *et al.* gave also the air mass (AM) 1.5 solar-emission spectrum. a-SiH$_{0.16}$ is amorphous hydrogenated Si and x-Si is crystalline Si. [1]

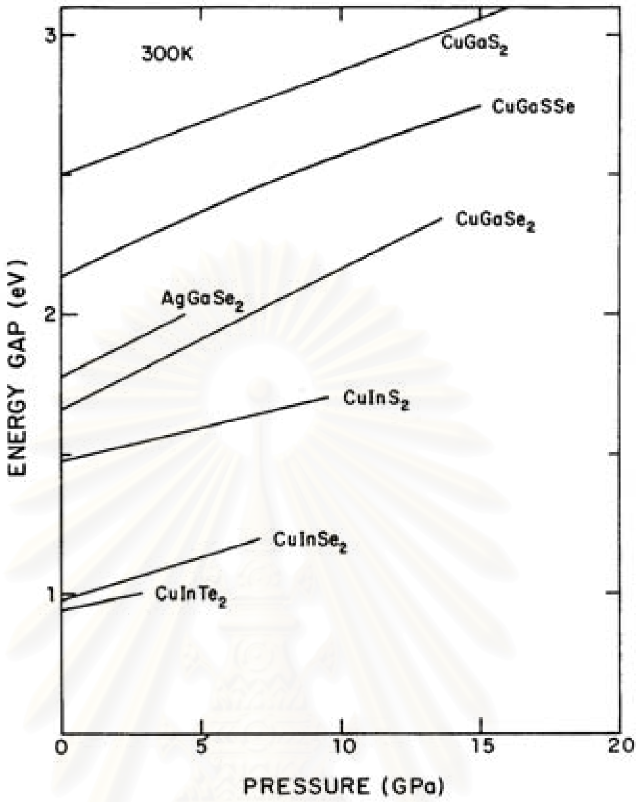

Figure 2: Pressure dependence of the direct energy gap in the ternary-compound semiconductors was shown by González *et al.* in 1995 [3].

$CuInSe_2$ is smaller than other ternary-compounds as shown in Figure 2 [3]. In Figure 3, González *et al.* [4] have shown that the direct energy gap of $CuInSe_2$ increases linearly with pressure at the rate of 30 $meV{\cdot}GPa^{-1}$ or 3 $meV{\cdot}kbar^{-1}$. Figure 4 shows the pressure dependence of the absorption edge of $CuInSe_2$ reported by González *et al.*. Because several properties of $CuInSe_2$, mentioned earlier, are highly depend on hydrostatic pressure, this material is enormously interested in high-pressure research recently.

In the early 1980s, Diamond Anvil Cell (DAC) have been used for structural study of single crystal sample. Energy-dispersive X-rays diffraction is one of the most basic tools for the comprehension of materials under high-pressure. These

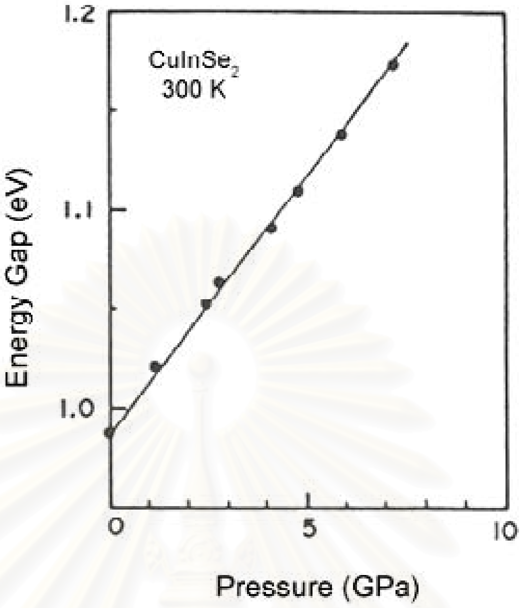

Figure 3: Pressure dependence of direct energy gap in CuInSe$_2$ was shown by González *et al.* in 1989 [2].

techniques have been extensively performed for a long period of time in high pressure crystallography. However, Energy-dispersive X-rays diffraction have limited resolution because of the unavoidable contaminations from sample-fluorescence lines and poor powder averaging due to the high degree of collimation between the sample and the detector. Both unavoidable contaminations and poor powder averaging have effect on peak intensities. To overcome this limitation, the resolution of reflections were improved by using x-rays from Synchrotron Radiation Source. Nevertheless, the unavoidable contaminant features still remain. Another technique of x-rays diffraction, Angle-dispersive X-rays diffraction was applied to tackle the contamination problems. The higher resolution of Angle-dispersive techniques can reduce the unavoidable contaminations from the sample and the detector. At this point, the resolution of reflections were improved but the problems arising from single crystal technique still remain. Since the single crystal sample could not survive intact through the abrupt density increase during

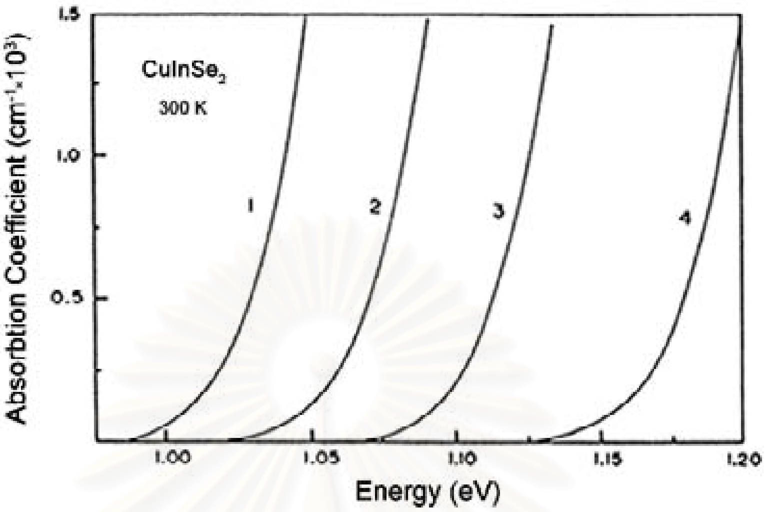

Figure 4: Shift in the absorption edge with hydrostatic pressure for CuInSe$_2$: (1) 12 kbar, (2) 28 kbar (3) 47 kbar, and (4) 71 kbar was shown by González *et al.* in 1989 [2].

applying high pressure, the single crystal sample is replaced by the polycrystalline powder sample. X-rays powder diffraction techniques are used for characterizing samples in the form of loose powders or aggregates of finely divided materials. These techniques cover with various investigations including qualitative and quantitative phase identification and analysis; crystallinity, microstructure, and lattice parameter determinations; high-temperature studies, and, in some cases, full crystal structure analysis. Not only to perform such identifications more simply, conveniently and routinely than any other analytical methods but the x-rays powder diffraction can also explain its importance in many industrial applications as well as its wide availability and prevalence [5].

In 1991, the Image-Plate method for high-pressure x-rays powder diffraction experiments with diamond anvil cell and Synchrotron Radiation was pioneered by O. Shimomura *et al.* at the Photon Factory in Japan [6]. Their beamline setup is shown in Figure 5. The Image-Plate is found to be more effective than a

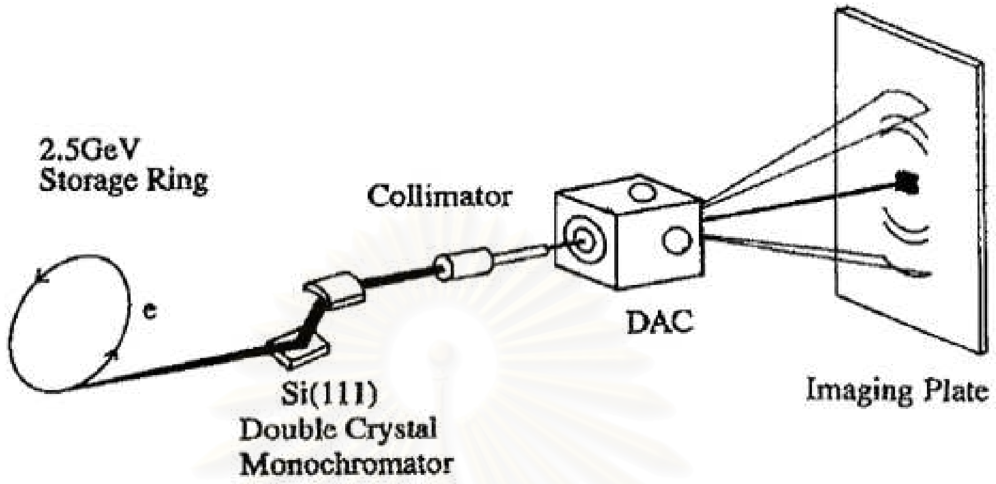

Figure 5: Schematic drawing of the setup for the combination of SR, DAC, and Image-Plate at the Photon Factory in Japan is shown [6].

conventional x-rays film because of its ideal characteristics for recording powder diffraction patterns. The advantages include low intrinsic noise, high sensitivity, high dynamic range, high absorption coefficient, a large size recorder and ease to operate. The intrinsic noise of Image-Plate is lower than those of photographic film about 300 times. Its sensitivity is about 10 photons per pixel ($\sim$0.1$\times$0.1 mm^2) for weak reflections. Its dynamic range is in the order of $\sim 10^5$ and its size is large enough to record a large part of complete 2-dimensional patterns without any reduction in resolution. The 1-dimensional data, required for crystal structure solving and full refinement, is simply obtained by integrating the 2-dimensional pattern around the rings.

The important things have been the ability to detect and characterize the microstructure effect of the sample. In high-pressure research, when the powder sample is pressurized, preferred orientations occur. Preferred orientation can cause a strong reflection to be clearly absence in a powder diffraction pattern and introduce large uncertainties into the structure solution and refinement [7].

Rietveld refinement can overcome a serious impediment to accurate crystallography by detecting and characterizing preferred orientation from its effects on 2-dimensional data [8]. By using Rietveld method, some other effects such as non-hydrostatic stress and stacking faults that cause displacing reflective planes can also be approached [9]. Moreover, we can distinguish the diffraction pattern of a multiple phase specimen simply by their texture and appearance [10].

The related theories for structural determination and refinement are given in chapter 2 which also include the details of many programs used for unit cell analysis and Rietveld refinement. Diamond anvil cell, Ruby fluorescence technique, and experimental method used in this research are implied in Chapter 3 and 4, respectively. Crystal structure analysis and discussion of $CuInSe_2$ under high-pressure phase are presented in Chapter 5. In Chapter 6, the conclusions are implied.

CHAPTER II

Structural Determination

2.1 X-Ray Powder Diffraction

X-ray powder diffraction (XRPD) is one of the most basic tools for the comprehension of material in the form of loose powders. The extensive use of x-rays for structural study of atomic arrangements and full crystal structure analysis is based on the fact that waves undergo diffraction. In this technique, a powdered specimen, which is random orientation of many crystallites, satisfy the diffraction conditions of Bragg's law [11]. In all instances, the radiation must have wavelengths in the range of 0.1 to 10 $\mathring{A}$ because the average distance between adjacent atoms in solid is about 1 $\mathring{A}$.

The incident beam of x-rays can be diffracted by crystals. Atoms scatter the incident x-rays in all directions and in some of these directions the scattered beams are completely in phase and so reinforce each other to form the diffracted beams. In Figure 6, the scattered rays are completely in phase and their path difference is equal to the n times of wavelengths, or if

$$n\lambda = 2d\sin\theta \qquad (1)$$

where n is called the order of diffraction corresponding to n = 1, 2, 3,... . This relation was first formulated by W. L. Bragg and is known as Bragg's law. It states the essential condition which must be met if the diffraction occurs. Therefore, for fixed values of wavelength λ and interplanar spacing d, there may be several angles of incidence θ_1, θ_2, θ_3,... at which diffractions may occur. In a first-order reflection (n = 1) of Figure 6, the scattered rays 1' and 2' would differ in length of path and in phase by one wavelength. The angle between the diffracted beam and the transmitted beam is always 2θ, known as the diffraction angle or Bragg angle. The rays, which are scattered by all the atoms in all planes,

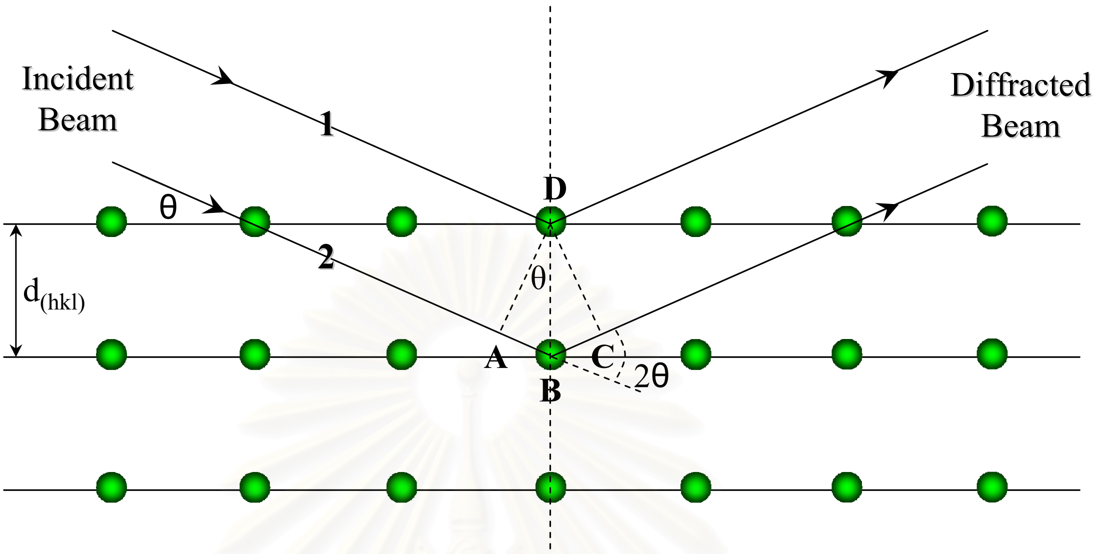

Figure 6: Bragg's Law

are completely in phase and reinforce one another to form a diffracted beam. For other directions of space the scattered beams are out of phase and cancel one another. The intensity of the diffracted beam depends on the arrangement of atoms on these planes. The diffracted beam is rather strong when all rays scatter in the same direction. Since the atoms of a crystal scatter only a small fraction of the incidented energy, the diffracted beam is extremely weak.

The powder diffraction pattern can be recorded with a detector-photographic film, charge-coupled device (CCD), image plate, position-sensitive photodiode (PSD), etc [12]. Whether the analog or digital data collection technique is used, the final data can be displayed as intensity profiles versus interplanar spacing or Bragg angle 2θ. Many modern x-ray powder diffractometer are equipped with data reduction and peak fitting facilities (finding peak intensity versus interplanar spacings and Bragg angles). A powder diffraction pattern of single phase material depends on the size and shape of its unit cell. When the symmetry of materials decreases, its powder diffraction pattern becomes more complex. For a powder pattern of multiple phases material, the pattern is more complex because all individual patterns from each phases are overlapping. The very low symmetry and large unit cell dimensions of the mixture cause complexity in the pattern too [5].

2.2 Image-Plate Method

Originally the diffraction pattern from x-rays diffraction was recorded by an x-rays camera which was designed to hold a specimen and photographic film for recording the diffracted beams. However, most of photographic films are sensitive to visible light. Therefore, the solid state area detector, called image plate, has been developed.

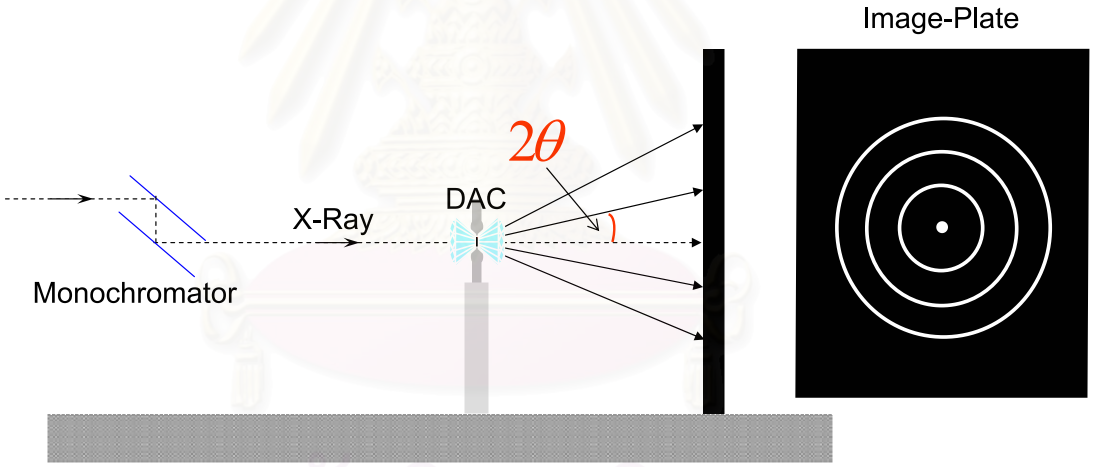

Figure 7: Image-Plate Method in high-pressure research are shown.

Image-Plate area detector is the reusable two-dimensional diffraction patterns recording media. The detection surface can be spherical, cylindrical, or flat. Both spherical and cylindrical area detectors are designed for a fixed sample to detector distance, while the flat area detector has the flexibility to be used at the different sample to detector distance, short distance for higher angular coverage and large distance for higher resolution [13]. This technique was originally developed for the medical radiology and has become very popular in high-pressure angle dispersive powder diffraction technique because the image-plate is sensitive for the short-wavelength ($\lambda < 0.7\ \mathring{A}$) which pass throughout the pressure cell [14]. The family of compounds comprising BaFX:Eu^{2+} (X = Cl, Br) has been known to have the high luminescence efficiency for x-ray excitation for over thirty years [16]. In this research, the phosphor materials BaFBr:Eu^{2+} have been bonded on the backing plate that made from a 20×25 cm^2 flat aluminium to be the fluorescence sensitizing screens and covered with a thin layer of transparent plastic.

When the x-ray photons are absorbed by phosphor screen, the excited electron state occur. After that He-Ne laser, $\lambda = 632$ nm, is used for irradiating the Image-Plate to generate the photostimulated luminescence in the visible light photon at $\lambda = 400$ nm. The intensity of visible light photon is proportional to those of original x-rays photon.

In high-pressure diffraction experiments, the background intensities of the diffraction are comprised of air scattering and pressure transmitting medium scattering. In the diffraction pattern, sometime, the contributions of at least two additional crystalline phases from the diamond anvils and the pressure calibration standard are presented [15]. In the diamond anvil cell, diamond can be recognized as a large single-crystalline so its contributions in the diffraction appear very intense and broad spots as shown in Figure 8(a). The ruby fluorescence technique is used for pressure measurement. In this techniques, the size of ruby crystal is as small as the average grain size of poly crystalline sample. Therefore, the ruby spots in diffraction pattern have approximately the same intensities as diffraction rings of the powder specimen as shown in Figure 8(b). The multiple phases from impurities and overlapping peaks in powder diffraction pattern can be treated by Rietveld refinements. In this way, the most accurately peak intensities can be extracted from the powder pattern for isolating peaks and overlapping peaks [15].

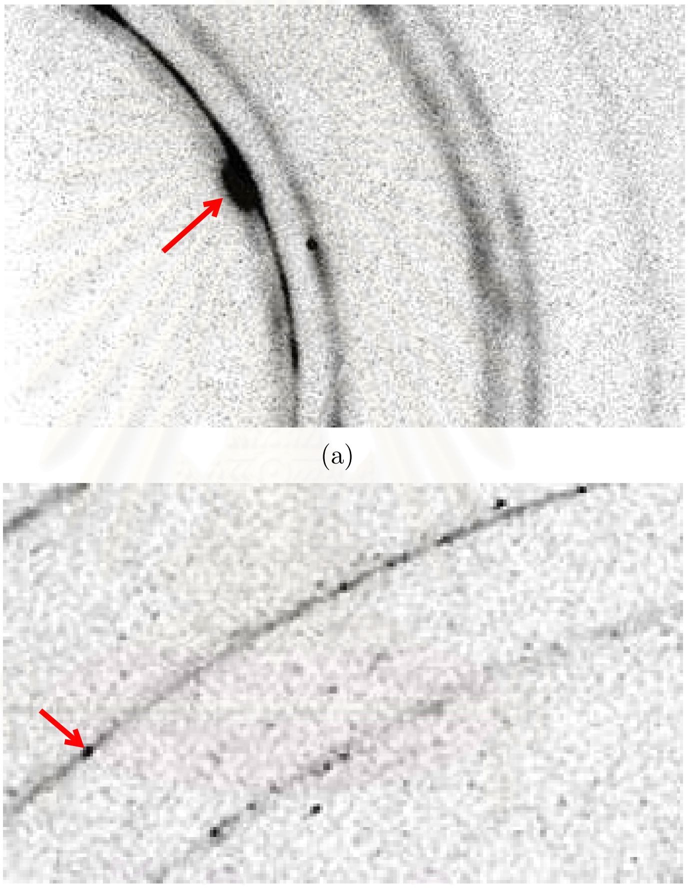

(a)

(b)

Figure 8: The image plate of $CuInSe_2$ with impurity spots in (a): Diamond is seemed as the large single-crystalline and their contributions in the diffraction appear very intense and broad spots, (b): The ruby spots in diffraction pattern have approximately the same intensities as diffraction spots of the sample.

2.3 Crystal Structure Refinement

First of all, the reflection peak intensities versus Bragg angle 2θ from the powder diffraction data were fitted for the lattice paremeters determination by using Gaussian and Lorentzian functions (Pseudo-Voigt) in the XRDA3.1 program. The "XRDA3.1 - a program for XRD analysis" [17, 18] was developed by Serg Desgreniers and Ken Lagaree at the Laboratoire des solides denses de I'Universite' d'Ottawa. This program was designed to simplify and speed up the analysis of multiple x-rays diffraction data. In addition, this program can also be used as the x-rays data management, peak profile fitting and diffraction intensity calculation.

Next, the "DICVOL91 - The automatic indexing of powder diffraction patterns variation of parameters" [19] and the "UNITCELL - refinement from powder diffraction data" [20] programs are used for determining the unit cell of $CuInSe_2$. The DICVOL91 was created by A. Bolutif and D. Louer of the University of Rennes, France to index powder diffraction patterns of low symmetry lattice, the cubic end of the symmetry sequence to triclinic lattices, by the successive dichotomy method [21]. The dichotomy method is base on the variation, in the direct space, of the lengths of the cell edges and interaxial angle by finite ranges. These parameters are progressively reduced by a dichotomy procedure if they contain possible solution. The UNITCELL has been developed by T.J.B Holland and S.A.T. Redfern at Department of Earth Sciences, University of Cambridge, to refine all parameters by minimizing residuals in the experimentally determined Bragg position in the terms of $2\theta_{hkl}$, d spacing (d_{hkl}) or energy (E_{hkl}) using a nonlinear least squares method.

After the lattice parameters were determined, the possible space group of the crystal and atomic coordinates were approximated by using the "CrystalCracker" which was developed by Kurt Leinenweber at Arizona State University, USA.

The CrystalCracker provides various manual techniques for solving the powder diffraction patterns. This program allows user to adjust with free of change in Bravais lattice, extinction symbol and lattice parameters for a crystal. In addition, this program allows the calculated line positions and collected data from monochromatic x-rays diffraction pattern to be compared.

The Rietveld method was first presented by H. M. Rietveld in 1969 [22]. Since the peak intensities depend on the atomic types and their distribution within the unit cell, the parameters actually being refined in this method are parameters in the models for the structure, intensities of Bragg peaks, and instrument effects on the diffraction pattern. The factors that affect the shape of reflection peaks are temperature, polarization, absorption, particle size, and preferred orientation so the fitting of reflection peak intensities throughout the whole diffraction pattern diagram will provide the accurate structural information of our sample. The least-squares refinements are used for adjusting the parameters of the model which compare the calculated diffraction profile with the observed step profile point by point. This method calculate intensities of the reflection peaks in the experimental pattern and combine it with various controllable factors in the form of diffraction diagram. Moreover, this model is adjusted to obtain the best fit and accurate information of the atomic positions in the unit cell. The usual refinable parameters are listed by classing Table 1 [23]. The calculated model can also describe many variables about the sample such as lattice parameter, symmetry of unit cell, atomic coordinates, thermal parameters, occupancy, optics, set-up of diffractometer, and peak shape, etc. Each variable is refined until the diffraction pattern from observing and calculating diagram are matched.

Table 1: Parameters refinable simultaneously [23]

For *each* phase present
x_j y_j z_j B_j N_j
(x_j, y_j, and z_j are position coordinates, B_j is an isothermal parameter, and N_j is the site-occupancy multiplier, all for the jth atom in the unit cell.)
Scale factor
Lattice parameters
Thermal parameter
Preferred orientation
Crystallite size and microstrain
Global
2θ-Zero
Instrumental profile
Profile asymmetry
Background
Wavelength
Specimen displacement
Specimen transparency
Absorption

The quantity minimized in the least-squares refinement is the residual, χ^2,

$$\chi^2 = \sum_i w_i (y_{oi} - y_{ci})^2 \tag{2}$$

where w_i = the statistical weight at the ith step, $\frac{1}{y_{oi}}$,

y_{oi} = the observed intensity at the ith step,

y_{ci} = the calculated intensity at the ith step,

and the sum is overall data points. The calculated intensity is a combination of many factors following the equation:

$$y_{ci} = s \sum_K L_K \mid F_K \mid^2 \varphi(2\theta_i - 2\theta_K) P_K A + y_{bi} \tag{3}$$

where s = the scale factor,

K = the Miller indices, $h\ k\ l$, for a given Bragg reflection,

L_K = the Lorentz factor,

φ = the reflection profile function,

P_K = the preferred orientation function,

A = an absorption factor,

F_K = the structure factor for the Kth Bragg reflection,

y_{bi} = the background intensity at ith point, can model or subtract, base on physical reality.

The reflection profile function approximates the effects of instrument and specimen features e.g. aberrations due to transparency, specimen displacement, and specimen-caused broadening [23]. The parameters which are not included in equation (3) are structural parameters and unit cell parameters (a, b, c; α, β, γ). In equation (3), $\mid F_K \mid$ depends on the positions of every atoms within each Miller plane and can be written as,

$$F_{hkl} = \sum_j N_j f_j \exp\left[2\pi i(hx_j + ky_j + lz_j)\right] \exp\left(-B \sin^2 \frac{\theta}{\lambda^2}\right) \tag{4}$$

where N$_j$ = the site occupancy,

f_j = the structural factor for jth atom,

x_j, y_j, z_j = the position parameters of jth atom in the unit cell,

B = the thermal vibration.

The peak shape in the powder diffraction can be described by Gaussian and Lorentzian functions (pseudo - Voigt) with the refinable degree of mixing following the equation:

$$pV = \eta L + (1-\eta)G \tag{5}$$

where pV = the pseudo - Voigt function,

L = the Lorentzian function,

G = the Gaussian function,

η = the mixing parameter.

The mixing parameter can be refined as a linear function of 2θ however the refinable variables are NA and NB,

$$\eta = NA + NB * (2\theta). \tag{6}$$

and

$$NB * (2\theta)_i = \sum_{j=-n}^{n} NB_{i-j}(2\theta)_j \tag{7}$$

where $*$ = the convolution operation.

The peak shape also depend on the halfwidth of Bragg peaks or Full Width Half Maximum (FWHM). The FWHM shows an angular dependence that express by the Caglioti function,

$$H^2 = U\tan^2\theta + V\tan^2\theta + W \tag{8}$$

where H = the halfwidth of Bragg peaks (FWHM),

U, V, W = the refinable parameters.

After the specimen is pressurized in the diamond anvil cell, the crystallites in the powder sample tend to be oriented in one way more than all others; in this case the preferred orientation occurs. In powder diffraction experiments, the preferred orientation, which is a frequent problem, produce the systematic distortions of the reflection peak intensities. Those distortions can be model mathematically in the form of the preferred orientation function (P_K),

$$P_K = \exp\left(-G_1\alpha_K^2\right) \tag{9}$$

or

$$P_K = G_2 + (1 - G_2)\exp\left(-G_1\alpha_K^2\right) \tag{10}$$

where $G_1,\ G_2$ = refinable parameters,

α_K = the angle between $\boldsymbol{d}_K^*$ and the fibre axis direction.

This P_K is used for the small preferred orientation. In 1989, Ahtee *et al.* [24] presented the spherical harmonic formulation that also referred to an orientation distribution function defined a set of terms to treat the preferential orientation as a function of the sample and the Laue phase symmetry. There is only one set of terms that use for each phase, so this function should not be used with the different types of powder data.

A computer program, based on the described method and least-squares refinement, used in this research is the "GSAS - Generalized Structure Analysis System" program [25, 26]. The GSAS has been developed by Allen C. Larson and Robert B. Von Dreele at Los Alamos National Laboratory, USA. This program is widely used for fitting crystallographic and magnetic structural models to x-ray and neutron single crystal and powder diffraction data with both time - of flight and monochromatic neutron powder diffraction. In addition, it can also work with multiple phases, including mixed powder sample.

CHAPTER III

High-Pressure Techniques

3.1 Diamond Anvil Cell

Nowadays the diamond anvil cell (DAC) has been very useful in expanding the knowledge of physical world through scientific investigation of the properties of material under a wide range of pressures. The high pressure techniques can solve fundamental questions about the phase transitions, crystal structure, the nature of atomic bonding and the physical properties analyzing in the applied materials research [27]. Not only be used for high pressure techniques but the DAC can also be coupled with other condensed-matter techniques such as photoluminescence, Raman scattering, Brillouin scattering, X-rays diffraction and transport property measurements for various studies [28].

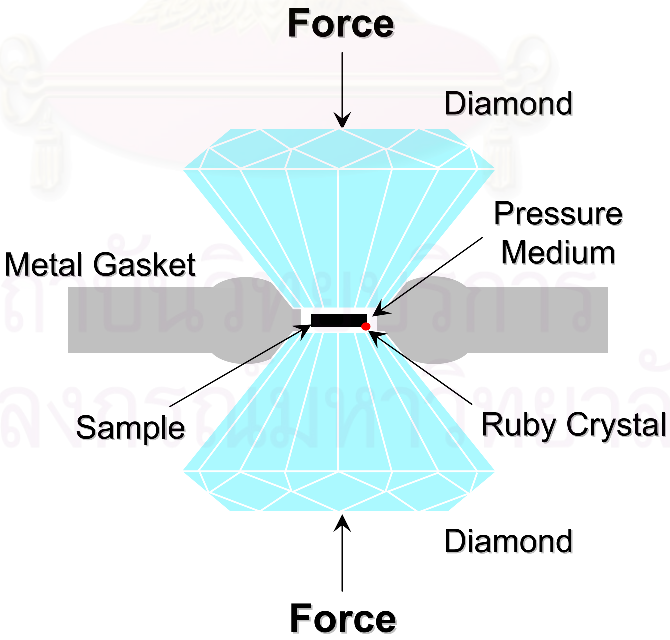

Figure 9: The main components of Diamond-Anvil Cell, with a metal gasket for confinement of the sample and pressure transmitting medium are shown.

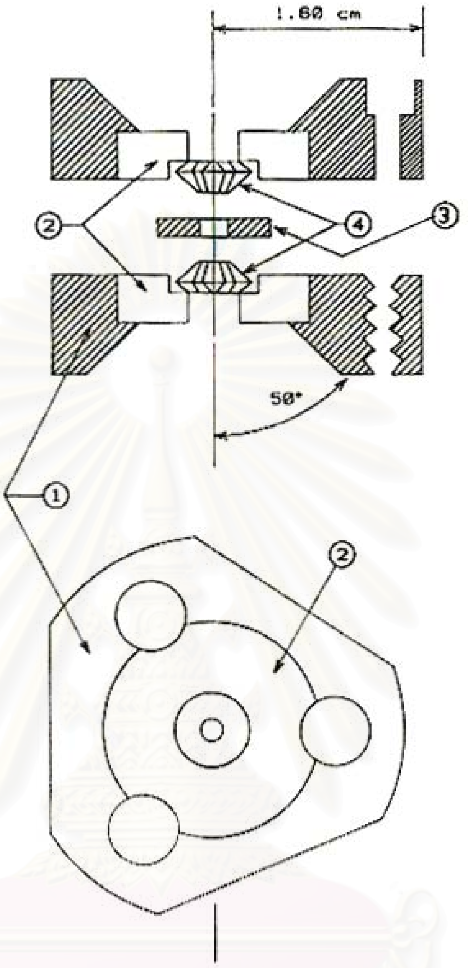

Figure 10: Schematic diagram of a Merill-Bassett (M-B) diamond-anvil cell [30] comprises of (1) Stainless steel body (2) Beryllium discs (3) Gasket (4) Diamond anvils.

The diamond anvil cell is a simple device capable of generating pressures almost as great as the pressure at the Earth core, 3,500 kbar. Figure 9 shows the main components of the DAC that comprise of a metal gasket, 2 diamond culets, powder sample, a ruby crystal and a pressure transmitting medium. A tungsten sheet is compressed between 2 diamond culets. A pressure transmitting medium, which is a mixture of 4:1 methanol: ethanol, and the pressure calibrant, which is a ruby crystal of ∼10 micron in size, are filled in a central hole of gasket. High pressures are generated in the pressure cell by taking a small force of the

Figure 11: DXR-6 Diamond-Anvil Cell is shown. Pressures of up to 950 kbar have been obtained with this cell type, using 200 micron anvil culets.

diamond culets to a small area by tightening the screws of the two beryllium discs together. The beryllium disc is used as supporting components in DAC as shown in Figure 10. Since the area of the culet is very small, about 0.01 mm^2; a modest load of force about 104 N is sufficient to generate a pressure in excess of 1,000 kbar. Diamonds are used as anvils because they are the hardest and least compressible material; and therefore they do not break or deform under such ultra force in pressure cell. In addition, diamond has the important property of being transparent to most of the spectrum of electromagnetic radiation including γ-ray, X-rays, portions of ultraviolet, visible and most of the infrared region [27].

In this research, x-ray diffraction is used for determining the crystal structure of $CuInSe_2$ under high pressure. The beryllium discs are used as a baking plate; since they are transparent to X-rays and allowing us to measure the diffraction from the sample [29]. Many diamond anvil cells have been designed in the different ways depending on the need and ingenuity of the designers. In this thesis, the DXR-6 pressure cell, Figure 11, is used to generate pressure.

3.2 Pressure Calibration

The most suitable and convenient technique of pressure measurement in DAC is Ruby - Fluorescence technique; since fluorescence spectrum of a ruby crystal in the diamond anvil cell shift to the lower energy with the increasing pressure as shown in Figure 12. Piermarini *et al.* (1975) [31] have reported the pressure dependence of the R_1 ruby fluorescence line which was calibrated at 25^oc against the compression $\frac{V}{V_0}$ of NaCl via the Dekker equation of state [32]. They have showed that its pressure dependence is linear up to 195 kbar following the equation:

$$P_{NaCl} = 2.746\Delta\lambda \tag{11}$$

where P is in kbar and $\Delta\lambda$ is the ruby R_1 line wavelength shift in $\mathring{A}$.

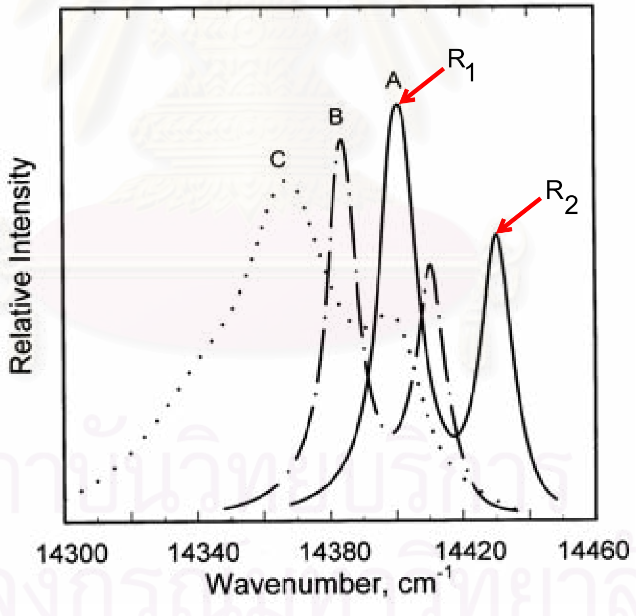

Figure 12: The R-line fluorescences of a ruby crystal in the DAC at room temperature are shown; ruby crystal: at ambient pressure (A); at about 22.3 kbar (B); at about 40 kbar (C). The pressure - shift is to lower energy with increasing pressure [34].

In 1978, Mao *et al.* [33] calibrated the wavelength shift with the pressure of the ruby R_1 line ($\mathring{A}$) in the diamond pressure cell from 60 to 1000 kbar under simultaneously making specific volume measurements of Cu, Mo, Ag, and Pd. They refered those results to isothermal equations of state which derived from shock - wave experiments. This can be written as

$$P\,(kbar) = \frac{19040}{B}\left[\left(\frac{\Delta\lambda}{\lambda_0} + 1\right)^B - 1\right] \tag{12}$$

where $\Delta\lambda$ is the ruby R_1 line wavelength shift in $\mathring{A}$. B = 7.665, 5 for quasi - hydrostatic and non - hydrostatic conditions, respectively. λ_0 is the wavelength measured at 1 bar in $\mathring{A}$ equal to 6942 for R_1 line and 6928 for R_2 line. The wavelength shift $\Delta\lambda$ of the fluorescence line versus pressure are showing in Figure 13.

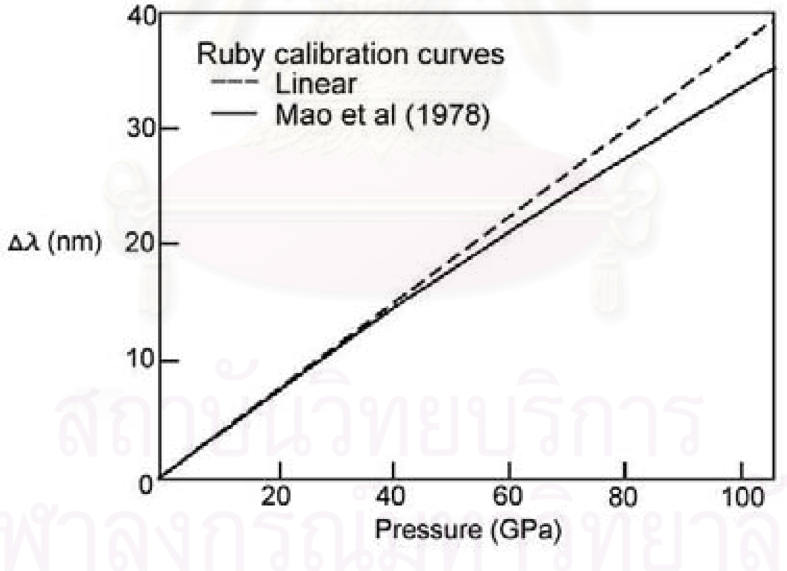

Figure 13: Plot of the wavelength shift $\Delta\lambda$ of the R_1 line fluorescence with pressure determined from the specific volume of Cu, Mo, Ag, and Pd. The dashed line is a linear extrapolation of the data from Piermarini *et al.* [31]. The solid line is a least - squares curve fit to the data points. [33]

CHAPTER IV

Experimental Methods

In this research, Angle dispersive X-rays diffraction (ADXRD) and Diamond-anvil cell (DAC) techniques are essential for crystal structure determination under high pressure. The DXR-6 diacell is used for this experiment. Tungsten sheet, used for the gasket material, is approximately 250 micron in thickness. The mixture 4:1 of methanol and ethanol is used as the pressure transmitting medium for hydrostatic pressure inside the DAC. Pressure is applied by squeezing the backing discs which support diamonds together.

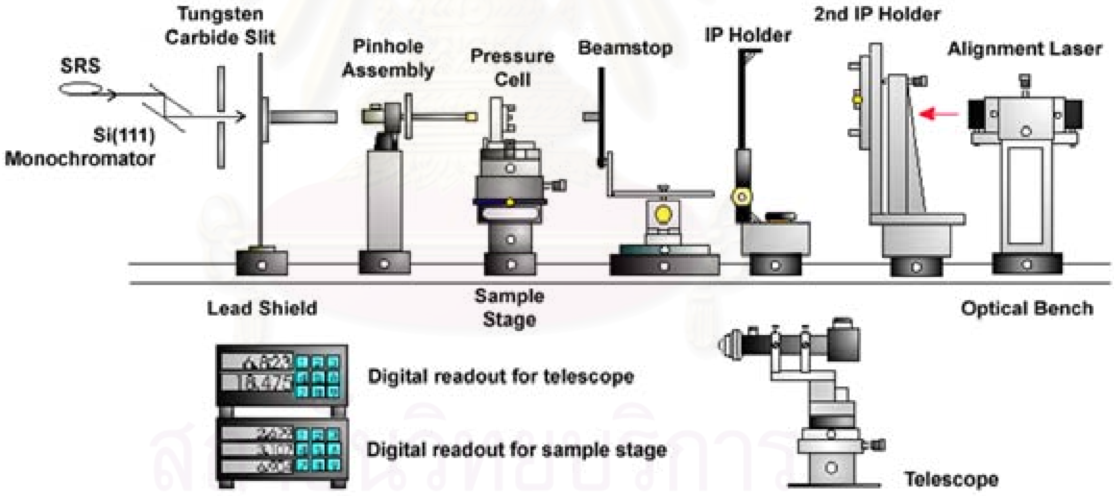

Figure 14: The beamline setup for high-pressure powder-diffraction on station 9.1 the SRS, Daresbury are shown [14].

X-ray powder diffraction data of $CuInSe_2$ were collected at the Synchrotron Radiation Source (SRS) at Daresbury Laboratory, UK [35]. The wavelength of x-rays from the SRS is 0.4654 $\AA$. The principal components of the current SRS beamline equipment on station 9.1 at SRS, Daresbury laboratory are shown in Figure 14. A double-bounce channel cut Si (111) monochromator is used for

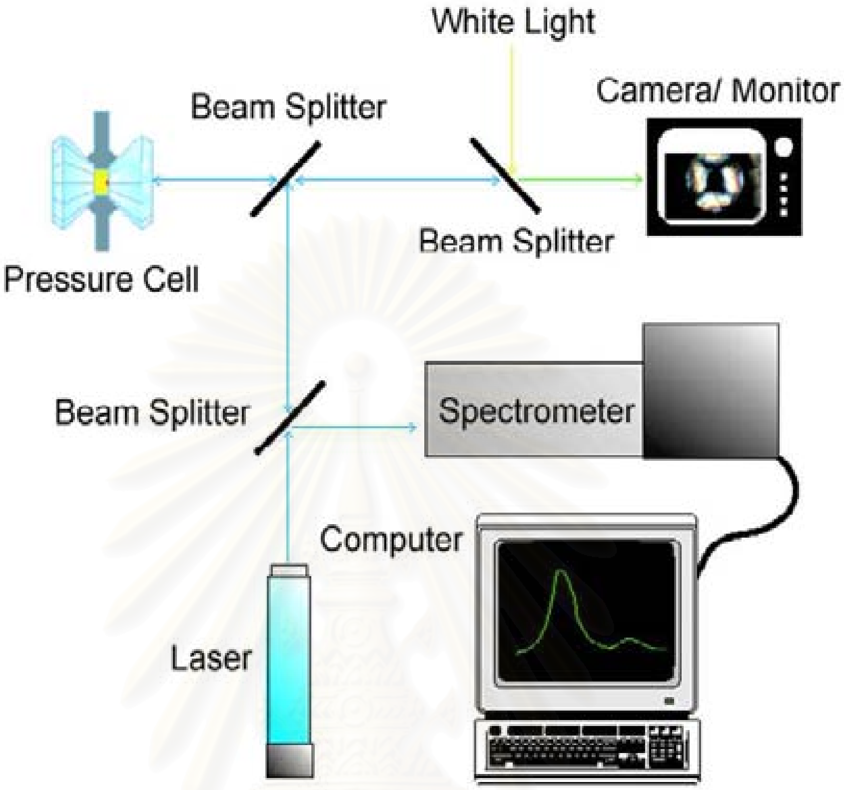

Figure 15: Schematic diagram shows the ruby pressure measurement equipment at SRS, Daresbury [14].

selecting the required wavelength for Angle dispersive x-rays diffraction. To reduce the dimension of the x-rays beam to 0.5×0.5 mm^2, we lay the tungsten carbide slit between monochromator and lead shield. A platinum pinhole is used for changing the shape of the beam to the circular beam 50-100 μm in diameter. The X-ray beam is perpendicular to the faces of the DAC and incident to the powder of $CuInSe_2$ inside DAC. After the beam pass through the DAC, the beamstop is used for protecting the Image-Plate (IP) detector from exceeding rays. The IP is made from the phosphor materials $BaFBr{:}Eu^{2+}$ on a sheet of aluminum in 20×25 cm^2 and all components are coverall with the transparent plastic to protect IP from reaction. To align the sample accurately on the X-ray beam, an optical method employed at Photon Factory [6] is used. The laser in

Figure 15 is used for marking the X-ray beam and aligning the components. The telescope is used for focusing on the sample through DAC and is removed during exposures.

The Ruby fluorescence technique is used for calibrating the pressure scale inside the DAC before and after x-ray powder diffraction data were collected. The pressure measurement system used at SRS Daresbury Laboratory is shown in Figure 15. The He-Cd laser use for stimulating electron inside the ruby crystal to emit the fluorescence. The fiber optics, which are the path of He-Cd laser, focus laser beam on a ruby crystal inside the DAC. After that the ruby fluorescence lines go out from the same path and go to the beam-splitter and spectrometer. The spectrum consists of the fluorescence in difference frequencies including ruby fluorescence and background signal. These fluorescence lines are dispersed by a grating onto a photo-diode array. After that those collected spectrums are complied by computer. The pressure inside the DAC can be calculated by using the shifting of R_2 line fluorescence following the equation (12).

CHAPTER V

Results and Discussions

In order to find the crystal structure and the phase transition of $CuInSe_2$, the x-ray powder diffraction data were collected under high-pressure at ambient temperature. At the beginning, powder sample of $CuInSe_2$ were measured under pressure range 0.001013 kbar or 1 atm to 87.73 kbar. At ambient pressure, the crystal structure of this material is tetragonal chalcopyrite with space group $I\bar{4}2d$ and lattice parameters a = 5.785(5) $\mathring{A}$, c = 11.616(9) $\mathring{A}$ and V = 388.846(1) $\mathring{A}^3$ as shown in Figure 16. The strong reflections of the pattern in this phase can be indexed to be (112), (204) and (312) as shown in Figure 17. The observed and

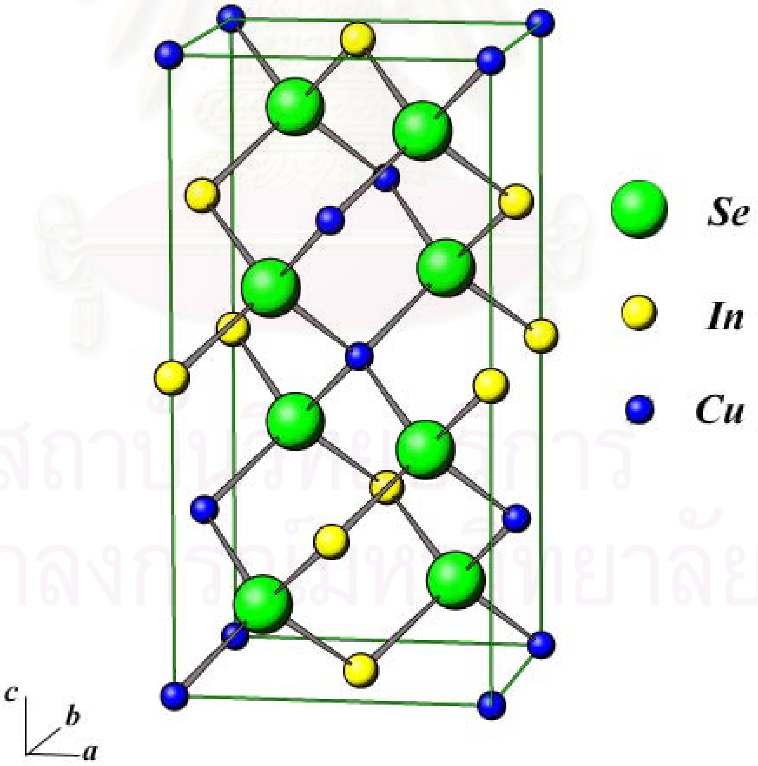

Figure 16: The crystal structure of $CuInSe_2$ at ambient pressure is tetragonal chalcopyrite with space group $I\bar{4}2d$ and lattice parameters a = 5.785(5) $\mathring{A}$, c = 11.616(9) $\mathring{A}$ and V = 388.846(1) $\mathring{A}^3$.

Table 2: Observed d spacings and 2θ angles (d_o and $2\theta_o$), and refined unit-cell dimensions for phase I of $CuInSe_2$ at 1.013 bar or ambient pressure and ambient temperature.

Present work at ambient pressure							
hkl	$d_c(\AA)$	$d_o(\AA)$	$\Delta d(\AA)$	$2\theta_c(^o)$	$2\theta_o(^o)$	$\Delta 2\theta(^o)$	I (%)
101	5.179	5.179(5)	0.0005	5.151	5.150(4)	-0.0006	3.04
112	3.344	3.344	0.001	7.979	7.979	0.000	100
103	3.218	3.220	0.002	8.294	8.288	-0.006	3.72
004	2.904	2.874	-0.030	9.191	9.287	0.096	0.61
200	2.893	2.822	-0.071	9.228	9.461	0.233	2.83
211	2.525	2.524(2)	-0.0008	10.574	10.579	0.005	1.9197
105	2.156	2.153	-0.003	12.392	12.410	0.018	0.52
204	2.049(5)	2.049(9)	0.0004	13.039	13.037	-0.002	53.35
220	2.045(5)	2.047(7)	0.0022	13.064	13.050	-0.014	25.34
301	1.902	1.901	-0.001	14.051	14.066	0.015	1.94
116	1.750	1.750	0.000	15.282	15.284	0.002	17.26
312	1.745	1.744	-0.001	15.326	15.339	0.013	31.29
215	1.728(7)	1.729	0.0003	15.472	15.467	-0.005	0.73
323	1.482	1.480	-0.002	18.063	18.091	0.028	0.16
008	1.452	1.451(2)	-0.00091	18.443	18.454	0.011	3.61
400	1.446	1.444	-0.002	18.516	18.542	0.026	5.46
217	1.397	1.396	-0.001	19.178	19.196	0.018	0.22
411	1.393	1.391	-0.002	19.232	19.258	0.026	0.34
316	1.329(8)	1.328(7)	-0.0011	20.156	20.173	0.017	12.65
332	1.327(6)	1.327	-0.0006	20.190	20.200	0.010	6.47
325	1.320	1.320(3)	0.0003	20.302	20.303	0.001	1.61
413	1.319	1.318(6)	-0.0004	20.319	20.329	0.01	1.32
307	1.258	1.257(4)	-0.0006	21.321	21.330	0.009	0.65
415	1.201	1.200(7)	-0.0003	22.341	22.350	0.009	0.74
228	1.184	1.183	-0.001	22.668	22.696	0.028	5.90

To be continued Table 3 ≫

Table 3: Observed d spacings and 2θ angles (d_o and $2\theta_o$), and refined unit-cell dimensions for phase I of $CuInSe_2$ at 1.013 bar or ambient pressure and ambient temperature. (Continued from Table 2)

Present work at ambient pressure							
hkl	$d_c(\mathring{A})$	$d_o(\mathring{A})$	$\Delta d(\mathring{A})$	$2\theta_c(^o)$	$2\theta_o(^o)$	$\Delta 2\theta(^o)$	I (%)
424	1.181(7)	1.181	-0.0007	22.713	22.745	0.032	13.59
431	1.151(4)	1.151(1)	-0.0003	23.320	23.346	0.026	0.16
1 1 10	1.117(5)	1.117(8)	0.0003	24.037	24.031	-0.006	1.54
336	1.115	1.115(1)	0.0001	24.095	24.090	-0.005	2.19
512	1.113(6)	1.113(1)	-0.0005	24.123	24.135	0.012	5.28
503	1.108(7)	1.108(1)	-0.0006	24.232	24.244	0.012	0.49
433	1.108(7)	1.108(1)	-0.0006	24.232	24.244	0.012	0.24
521	1.069(8)	1.070	0.0002	25.127	25.119	-0.008	0.38
a ($\mathring{A}$)	5.785(5)						
b ($\mathring{A}$)	11.616(9)						
V ($\mathring{A}^3$)	388.846(1)						
N_A	4						

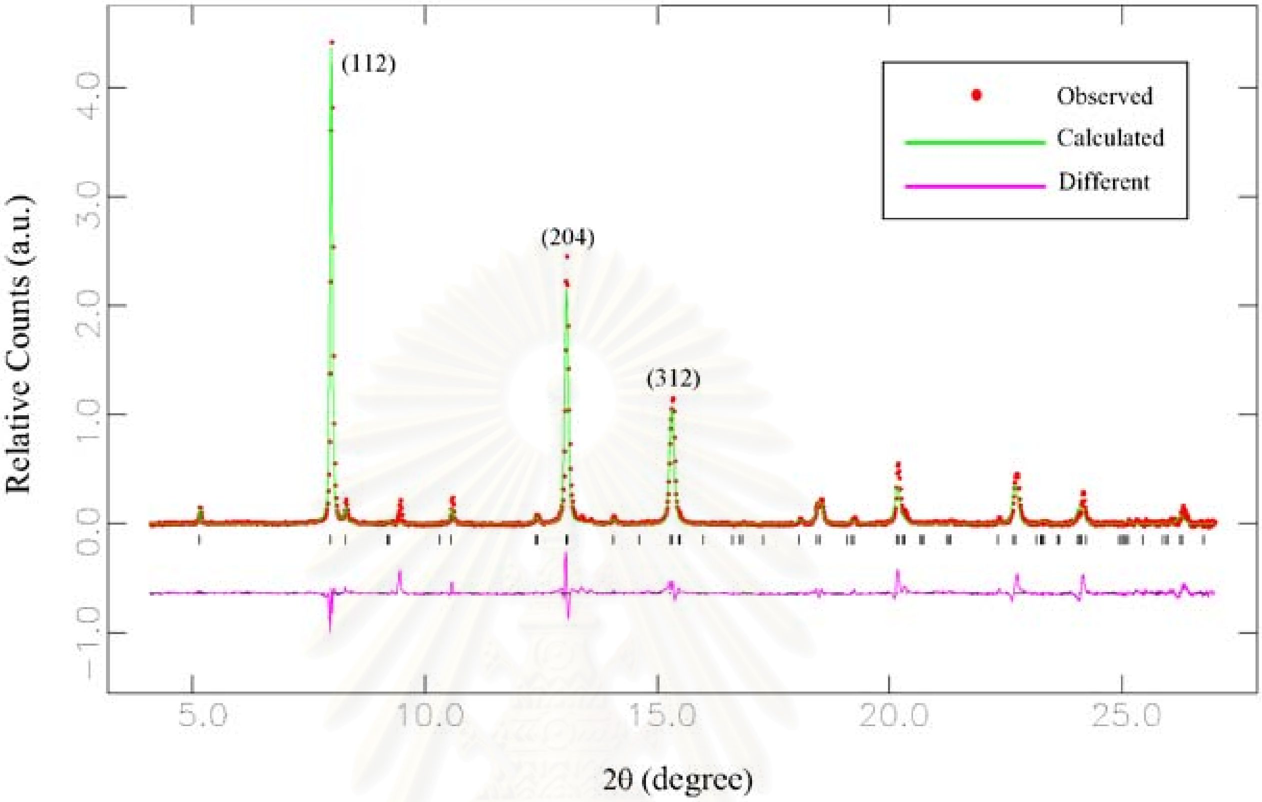

Figure 17: A diffraction pattern is recorded from the 1^{st} phase of $CuInSe_2$ at ambient pressure. The strong reflections are shown.

calculated d spacings for these (hkl) reflections are shown in Table 2 and 3.

With the increasing pressure, the volume of $CuInSe_2$ is decreasing and the change in its powder diffraction pattern is emerging. In Figure 18, no phase transition is observed between 27.46 and 61.77 kbar. Nevertheless, when the pressure increases gradually to 70.03 kbar, the tetragonal phase starts transforming to high-pressure phase. With a slight tightening of the pressure cell to 74.42 kbar, six reflections (circled) of the high-pressure phase appear very clearly. A mixture ratio of new phase:tetragonal phase at this pressure is 87:13. At 81.23 kbar the high-pressure phase reflections (circled) become stronger than the high-pressure phase reflections in the previous pressure level as shown in Figure 18 and a mixture ratio of new phase:tetragonal phase is 97.5:2.5. After that, the tetragonal

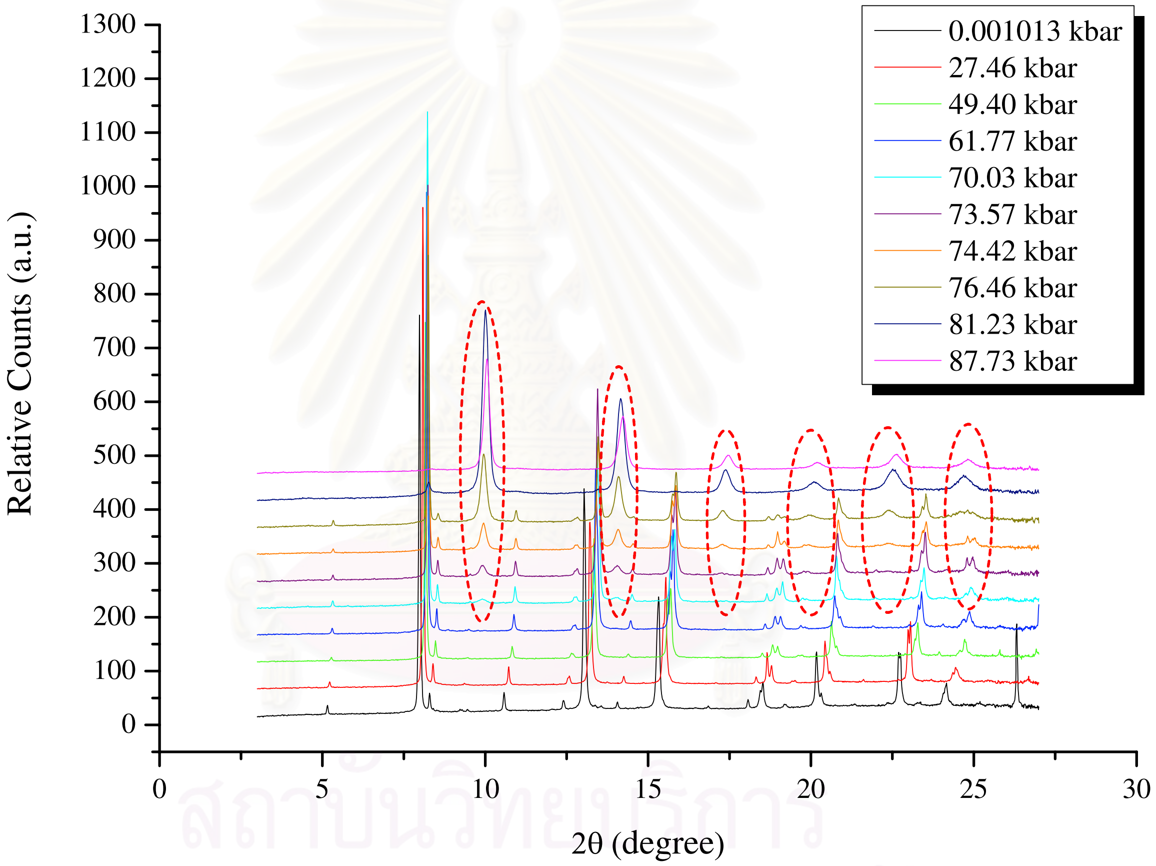

Figure 18: The diffraction patterns of $CuInSe_2$ at pressure between 0.001013 and 87.73 kbar are shown.

Table 4: Observed d spacings and 2θ angles (d_o and $2\theta_o$), and refined unit-cell dimensions for phase II of $CuInSe_2$ at 87.73 kbar and ambient temperature.

	Present work at 87.73 kbar						
hkl	$d_c(\AA)$	$d_o(\AA)$	$\Delta d(\AA)$	$2\theta_c(^o)$	$2\theta_o(^o)$	$\Delta 2\theta(^o)$	I (%)
111	3.069	3.209	0.140	8.697	8.318	-0.379	0.77
200	2.658	2.656	-0.002	10.046	10.052	0.008	75.76
220	1.879	1.878	-0.001	14.225	14.236	0.011	45.61
311	1.603	1.607	0.004	16.697	16.649	-0.048	0.21
222	1.534	1.532	-0.002	17.445	17.476	0.031	13.50
400	1.329	1.325	-0.004	20.170	20.227	0.057	8.06
331	1.219	1.218	-0.001	22.001	22.037	0.036	0.12
420	1.189	1.186	-0.003	22.580	22.622	0.042	16.34
422	1.085	1.084(9)	-0.0001	24.768	24.771	0.003	9.01
511	1.023	1.0184	-0.005	26.296	26.417	0.121	0.09
333	1.023	1.0184	-0.005	26.296	26.417	0.121	0.03
a ($\AA$)	5.315(6)						
V ($\AA^3$)	150.19(7)						
N_A	2						

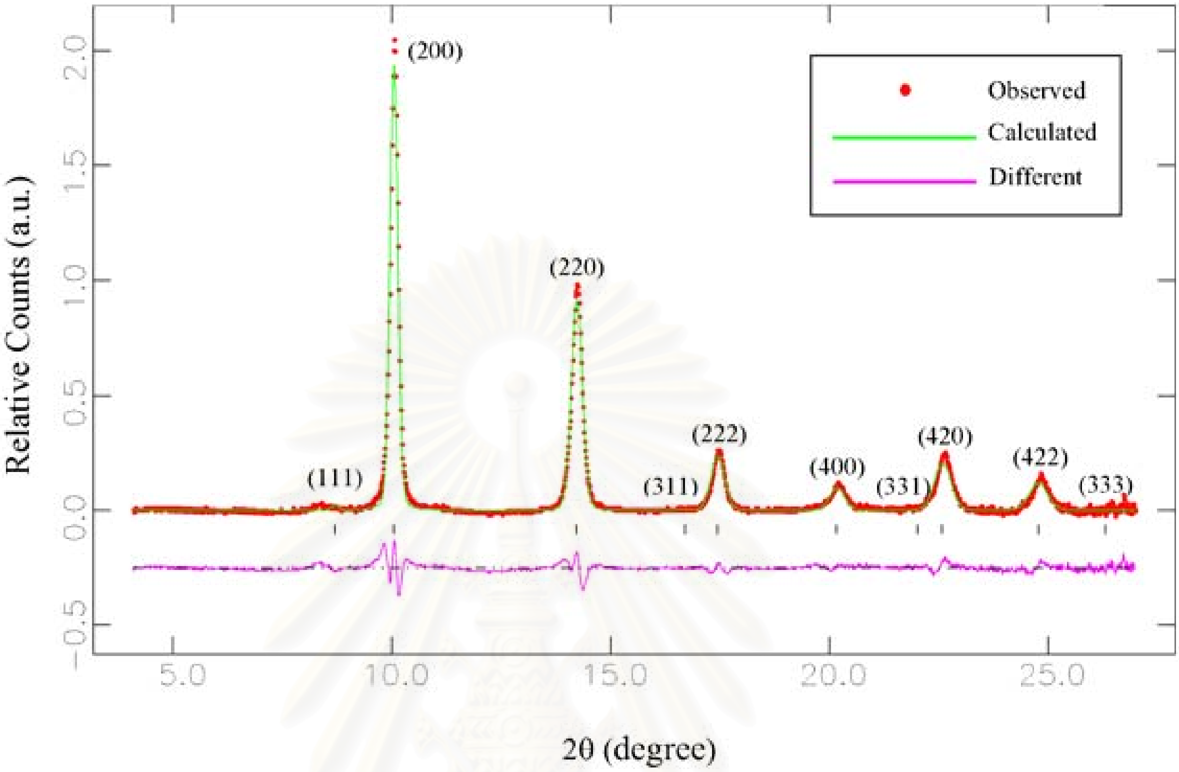

Figure 19: The diffraction pattern is recorded from phase II - cubic of $CuInSe_2$ at 87.73 kbar.

phase was completely transformed to the new phase, was called the phase II, when the pressure increases to 87.73 kbar.

The phase II of $CuInSe_2$ can be indexed by a cubic unit cell with (111), (200), (220), (311), (222), (400), (331), (420), (422) and (333) reflections in space group $Fm\overline{3}m$ or NaCl-like structure as shown in Figure 19. In this phase, the lattice parameters (a) equal to 5.315(6) $\mathring{A}$ and V = 75.098 $\mathring{A}^3$. In Figure 20, the reflection intensities of the phase II are well fitted with Cu-In atoms at (0.5, 0.5, 0.5) and Se atom at (0, 0, 0). There are disorder between Cu and In atoms in this phase with site occupancies of 50:50 for both atoms. Table 4 gives the observed and calculated d spacings for the (h, k, l) reflections in the phase II.

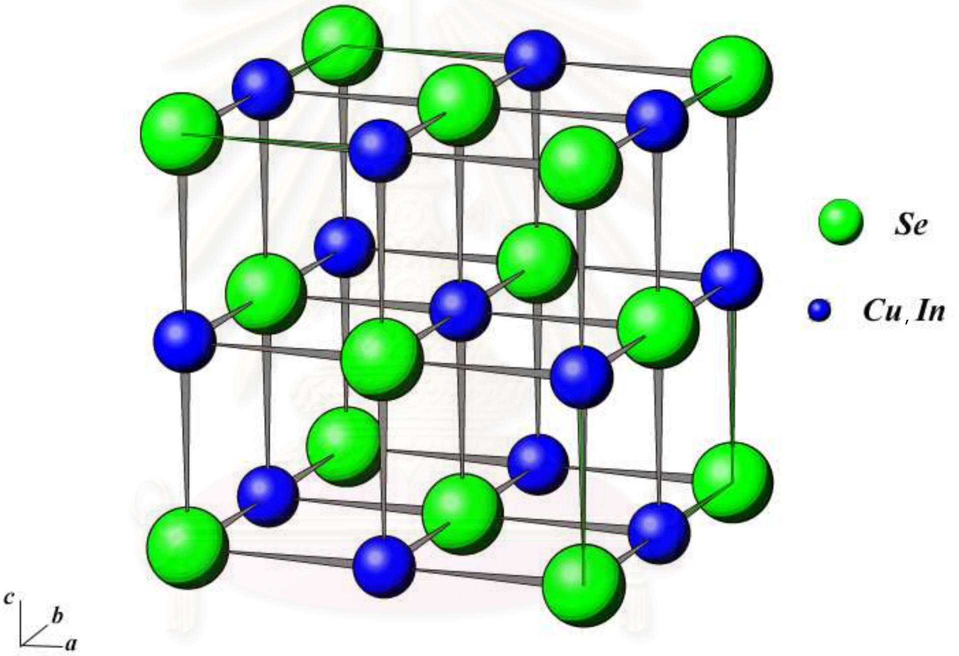

Figure 20: The crystal structure of $CuInSe_2$ at 87.73 kbar is cubic in space group $Fm\bar{3}m$ or NaCl-like structure with lattice parameters a = 5.315(6) $\mathring{A}$ and V = 75.098 $\mathring{A}^3$.

Subsequently, the high pressure powder diffraction data of $CuInSe_2$ were measured again for finding the third phase under the pressure range 0.001013 to 277 kbar. No transition is observed at the pressure between 0.001013 and 69.1 kbar. When the pressure goes up to 110.9 kbar, the tetragonal phase completely transforms to the cubic phase which is stable in the pressure range 110.9 to 277 kbar. However, the patterns collected in the pressure range 110.9 to 173.2 kbar were contaminated by the very weak (110) reflections (arrowed) of the tungsten gasket at $2\theta \sim 12^o$ as shown in Figure 21.

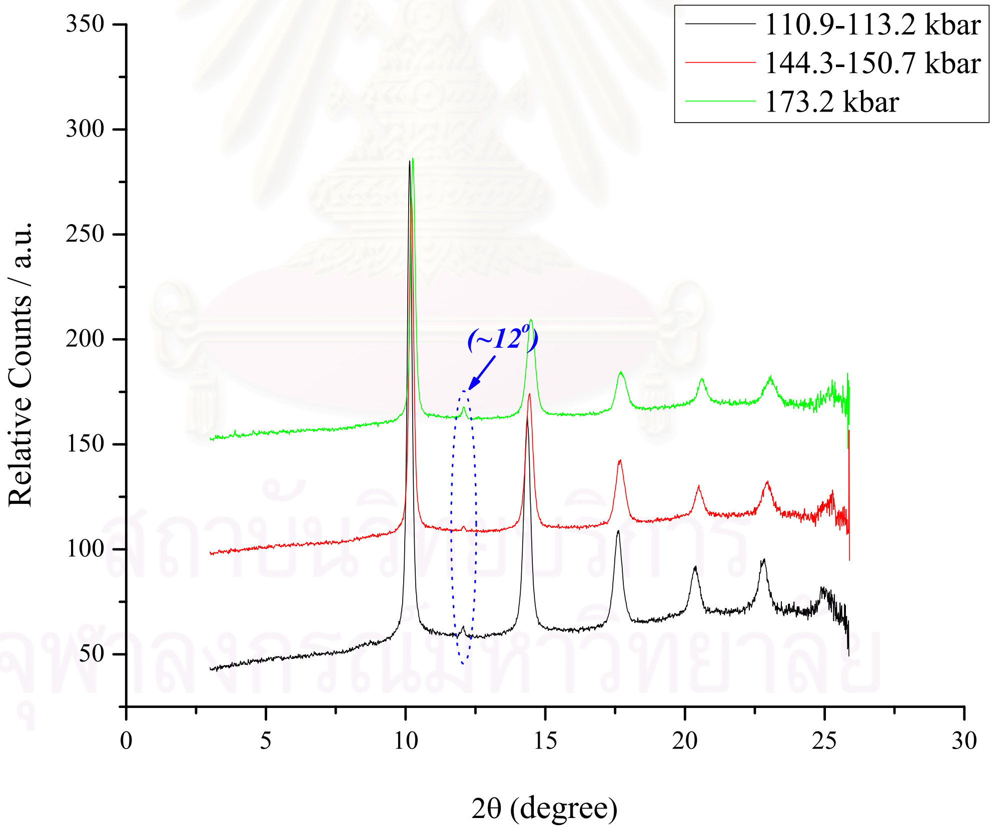

Figure 21: In the pressure range 110.9 to 173.2 kbar, the patterns were contaminated by the very weak (110) reflections (arrowed) of the tungsten gasket at $2\theta \sim 12^o$.

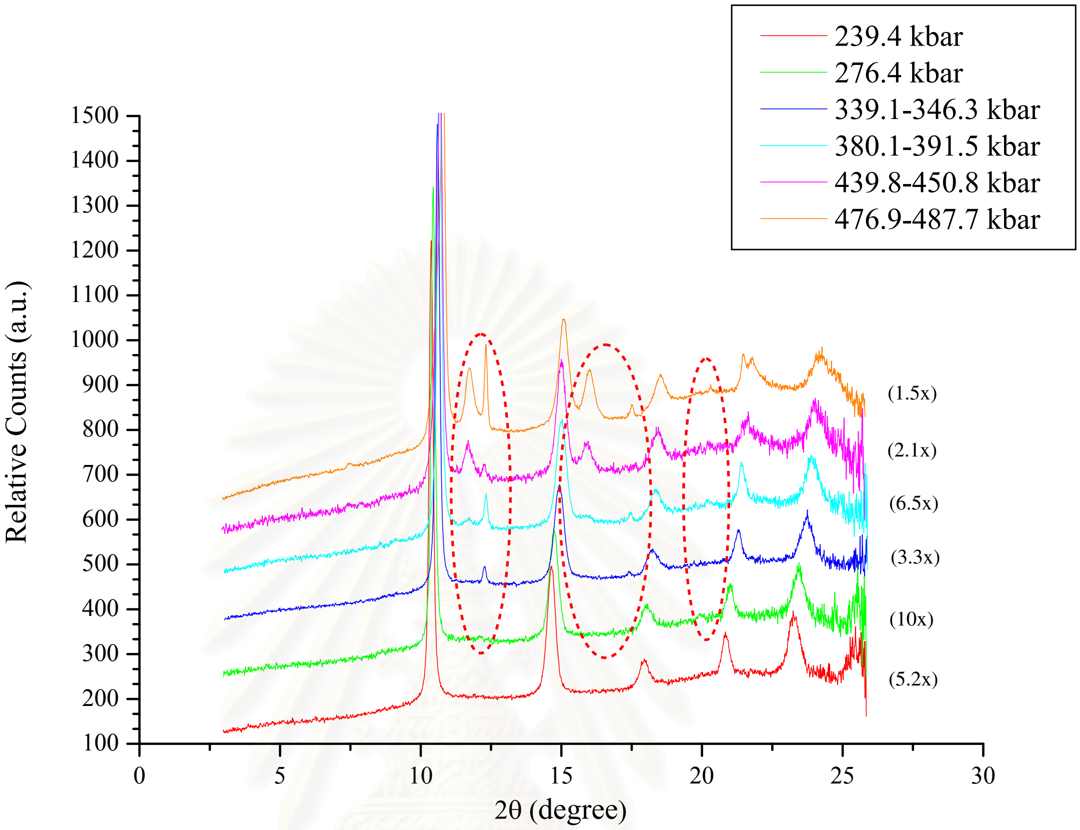

Figure 22: The diffraction patterns of $CuInSe_2$ at pressure range 239.4 to 532 kbar are shown.

In order to search for the phase III of $CuInSe_2$, the pressure was increased gradually to 532 kbar. No transition was observed between 110.9 and 276.4 kbar as shown in Figure 22. When the pressure increases to 339 kbar, the phase II begins to transform to the higher-pressure phase as shown in Figure 22. In this pressure range, there is overlapping of the (110) reflection line of the tungsten gasket and the new reflection at $2\theta \sim 12^o$ as shown in Figure 23. At 487.7 kbar, the reflections (circled) of the new phase are much stronger than those of the previous phase as shown in Figure 22. At the pressure between 439.8 and 450.8 kbar, one of the reflection (circled) for phase II at $2\theta \sim 21^o$ begin to split as shown in Figure 24. A 55:45 mixture of the new phase and the cubic phase is found at this pressure. In Figure 25, a 80:20 mixture of the new phase and the phase II was

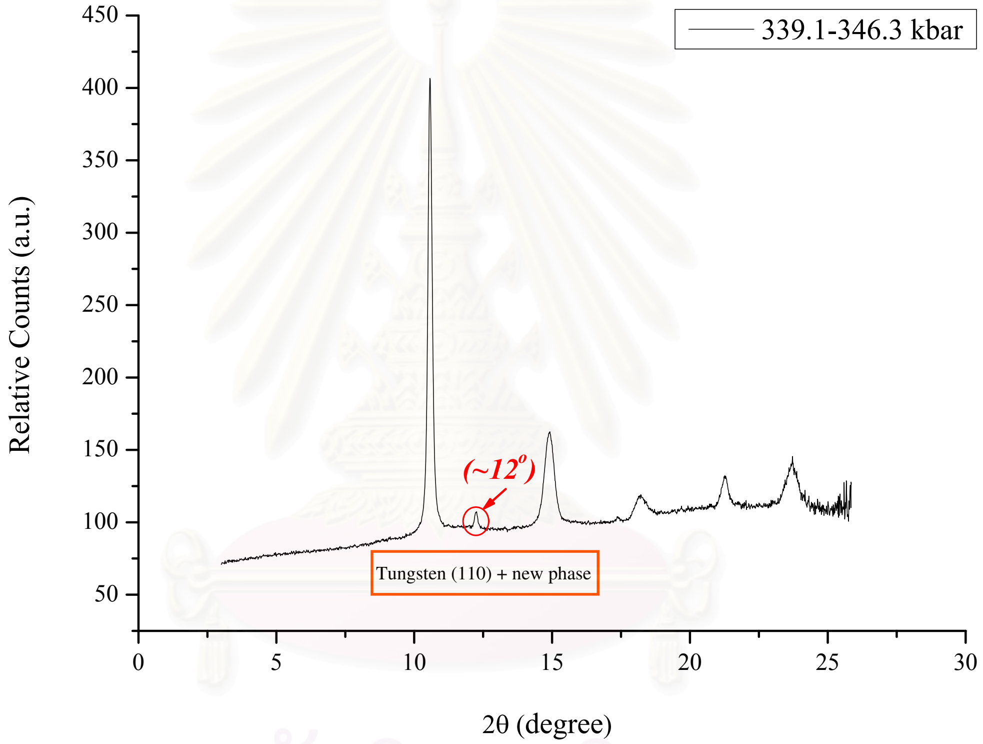

Figure 23: The diffraction pattern is recorded from $CuInSe_2$ at pressure range 339.1 to 346.3 kbar. The overlapping of the (110) reflection line of the tungsten gasket and the new reflection at $2\theta \sim 12^o$ is indicated by the circle.

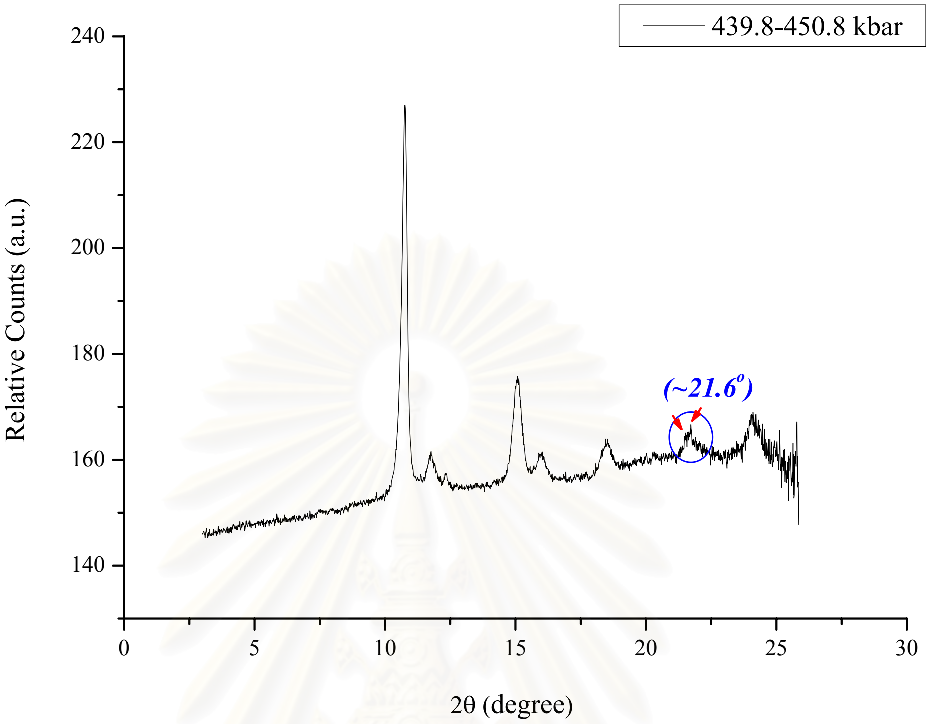

Figure 24: The diffraction pattern recorded from $CuInSe_2$ between 439.8 and 450.8 kbar. One of the reflection line (circled) of the phase II - *Cubic* phase at $2\theta \sim 21^o$ begin to split in the new phase.

refined at 476.9 kbar. The new reflections from phase III were clearly observed as indicated by red circled and arrowed. The (110) reflections (arrowed) from gasket at $2\theta \sim 12^o$ also appear in this pattern. In this pattern, we can confirm that this is the tungsten gasket reflection because its diffraction texture detected by the Image Plate is entirely different from others. The *Cubic* phase of $CuInSe_2$ was completely transformed to phase III at 532 kbar.

This new phase of $CuInSe_2$ can be indexed by the orthorhombic unit cell with space group *Cmcm* and lattice parameter a = 4.867(8) $\AA$, b = 5.023(8) $\AA$, c = 4.980(3) $\AA$ and V = 60.8973 $\AA^3$. The (110), (200), (021), (112), (221), (310), (222), (312), (331), (422) and (423) reflections are shown in Figure 26. In Figure 27, the calculated intensities of the crystal structure of $CuInSe_2$ in the phase III - orthorhombic are well fitted with the atoms at (0, y, 0.25), Cu-In

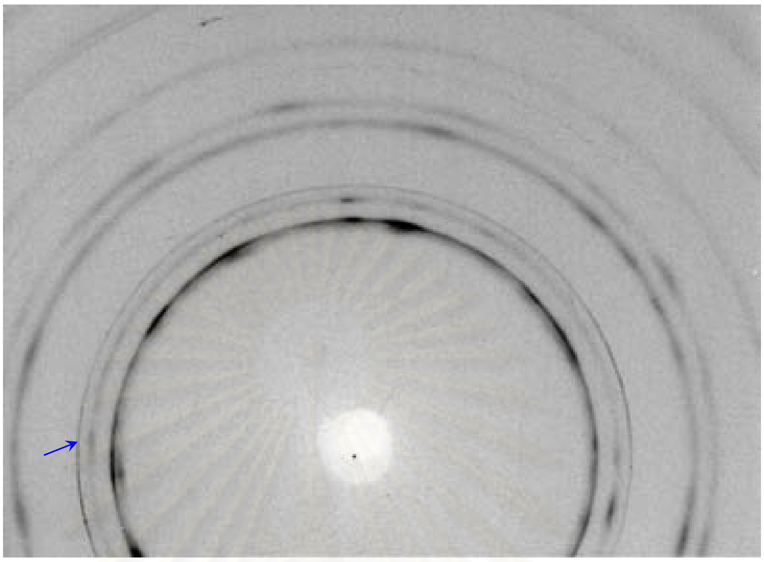

(a) The reflections of the high-pressure phase are shown.

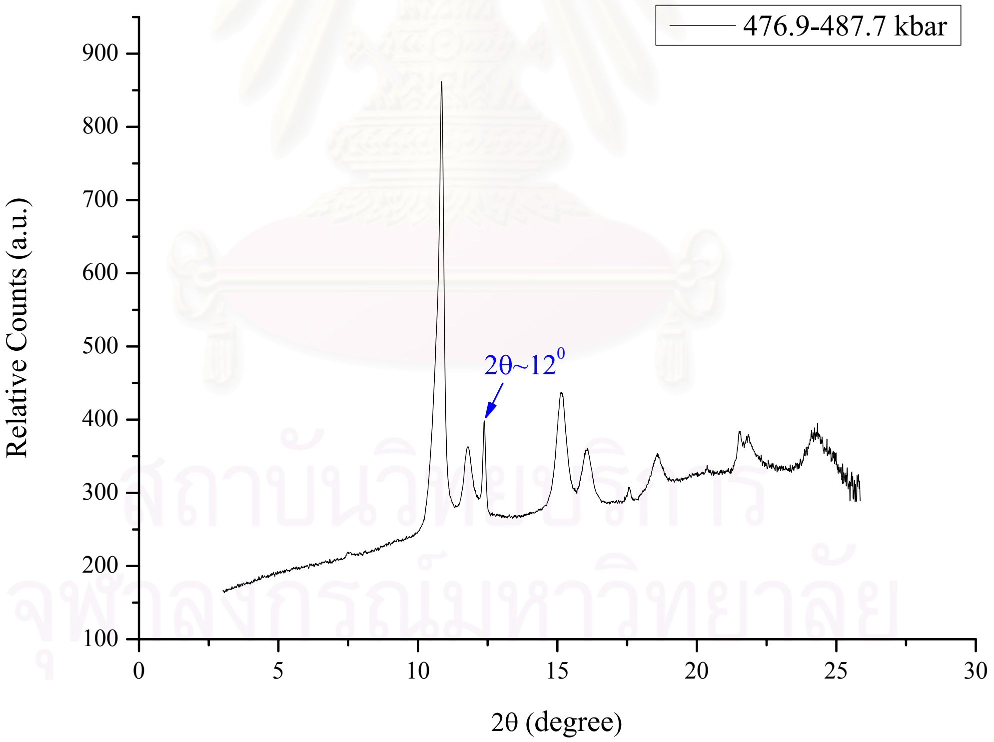

(b) The diffraction pattern of $CuInSe_2$ at pressure range 476.9 to 487.7 kbar.

Figure 25: The image-plate (a) and diffraction pattern (b) of the $CuInSe_2$ at pressure range 476.9 to 487.7 kbar. The strong (110) reflections (arrowed) of the tungsten gasket appears at $2\theta \sim 12^o$.

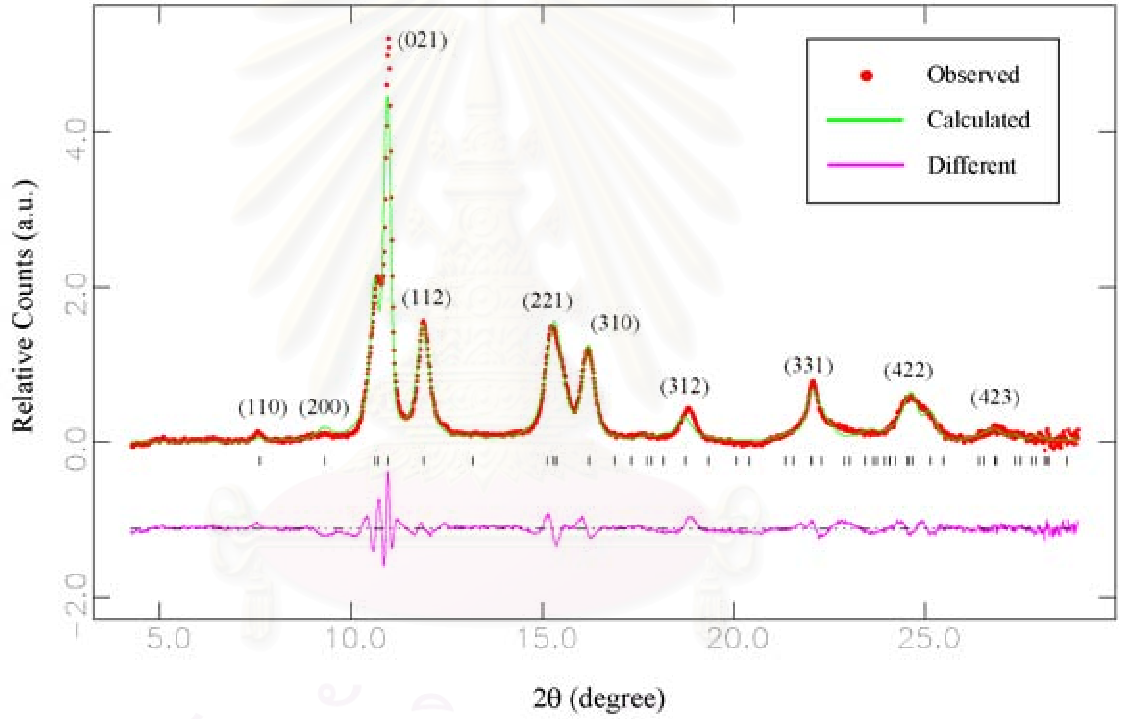

Figure 26: The diffraction pattern is recorded from phase III - *Cmcm* of $CuInSe_2$ at pressure 532 kbar.

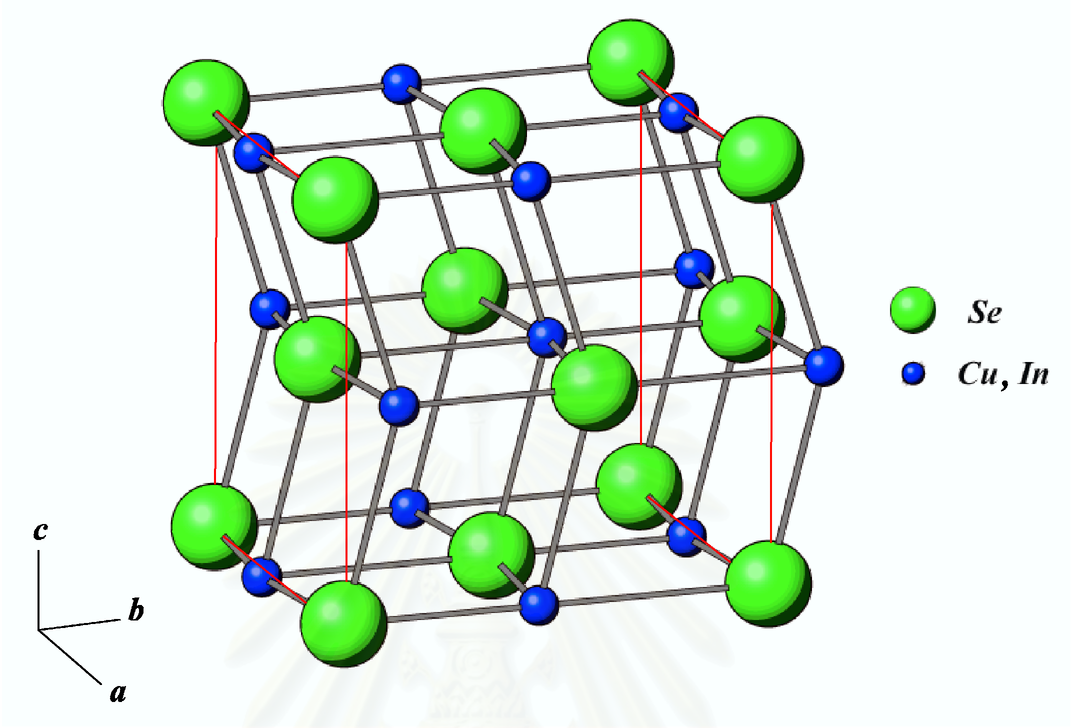

Figure 27: The crystal structure of $CuInSe_2$ at 532 kbar is orthorhombic unit cell with space group *Cmcm* and lattice parameters a = 4.867(8) $\mathring{A}$, b = 5.023(8) $\mathring{A}$, c = 4.980(3) $\mathring{A}$ and V = 60.8973 $\mathring{A}^3$.

atoms at y = 0.70, Se atom at y = 0.159(6). There are also disorder between Cu and In atoms in this phase with site occupancies of 50:50 for both atoms. Table 5 and 6 give the observed and calculated d-spacings for the (h, k, l) reflections in the phase III.

The high pressure structure solution of $CuInSe_2$ are *NaCl* and *Cmcm*, respectively. The *NaCl* structure is the well-known structure with six unlike nearest neighbors in each atom. The *Cmcm* structure is the base-centered-orthorhombic structure with lattice parameters $a \neq b \neq c$.

Table 5: Observed d spacings and 2θ angles (d_o and $2\theta_o$), and refined unit-cell dimensions for phase III of $CuInSe_2$ at 532 kbar and ambient temperature.

Present work at 532 kbar							
hkl	$d_c(\mathring{A})$	$d_o(\mathring{A})$	$\Delta d(\mathring{A})$	$2\theta_c(^o)$	$2\theta_o(^o)$	$\Delta 2\theta(^o)$	I (%)
110	3.496	3.536	0.040	7.633	7.546	-0.087	1.97
111	2.861	2.866	0.005	9.330	9.313(5)	-0.0165	6.10
020	2.512	2.514	0.002	10.631	10.621	-0.010	25.58
002	2.490	2.489(7)	-0.0003	10.724	10.725(8)	0.0018	100
200	2.433(9)	2.438(9)	0.005	10.972	10.949	-0.023	87.61
021	2.242(7)	2.251(7)	0.009	11.911	11.863	-0.048	77.70
112	2.028	2.024	-0.004	13.176	13.201	0.025	2.74
022	1.768(4)	1.768(7)	0.0003	15.122	15.120	-0.002	20.98
220	1.747(96)	1.748(0)	0.00006	15.301	15.300	-0.001	5.68
202	1.740(5)	1.739(5)	-0.001	15.366	15.375(6)	0.0096	86.98
221	1.649(3)	1.650(0)	0.0007	16.222	16.214(8)	-0.0072	55.25
131	1.509	1.508(7)	-0.0003	17.741	17.745	0.004	2.43
311	1.474(8)	1.475(3)	0.005	18.156	18.150	-0.006	1.74
222	1.430(7)	1.426(4)	-0.0043	18.722	18.778	0.056	21.33
023	1.385	1.386(7)	0.0017	19.345	19.320	-0.025	1.33
312	1.312(2)	1.312(1)	-0.0001	20.428	20.430	0.002	0.38
040	1.255(9)	1.255(6)	-0.0003	21.355	21.360	0.005	0.14
004	1.245	1.242(5)	-0.0025	21.544	21.587	0.043	7.42
041	1.217(8)	1.218(4)	0.0006	22.031	22.020	-0.011	9.51
400	1.217	1.216	-0.001	22.047	22.065	0.018	7.42
223	1.203(7)	1.203(1)	-0.0006	22.293	22.305	0.012	28.48
133	1.145(8)	1.146	0.0002	23.435	23.430	-0.005	6.58
331	1.134(6)	1.135(3)	0.0007	23.669	23.656	-0.013	2.25
042	1.121(4)	1.121(3)	-0.0001	23.953	23.955	0.002	0.26
240	1.116(1)	1.116(4)	0.0003	24.068	24.060	-0.008	0.86

To be continued Table 6 ≫

Table 6: Observed d spacings and 2θ angles (d_o and $2\theta_o$), and refined unit-cell dimensions for phase III of $CuInSe_2$ at 532 kbar and ambient temperature. (Continued from Table 5)

Present work at 532 kbar							
hkl	$d_c(\mathring{A})$	$d_o(\mathring{A})$	$\Delta d(\mathring{A})$	$2\theta_c(^o)$	$2\theta_o(^o)$	$\Delta 2\theta(^o)$	I (%)
204	1.108(5)	1.107(6)	-0.0009	24.237	24.255	0.018	11.09
402	1.093(3)	1.093	-0.0003	24.576	24.585	0.010	22.44
241	1.089	1.088	-0.001	24.674	24.690	0.016	12.11
421	1.069(6)	1.069(8)	0.0002	25.130	25.125	-0.005	15.69
224	1.014	1.013(9)	-0.0001	26.531	26.535	0.004	5.82
422	1.002(5)	1.002(8)	0.0003	26.843	26.835	-0.008	4.35
043	1.001(6)	1.002	0.0004	26.868	26.850	-0.018	4.11
a ($\mathring{A}$)	4.867(8)						
b ($\mathring{A}$)	5.023(8)						
c ($\mathring{A}$)	4.980(3)						
V ($\mathring{A}^3$)	121.794(6)						
N_A	2						

The difference in powder diffraction pattern of $CuInSe_2$ in *NaCl* and *Cmcm* phases can also be used to identify the crystal structures, e.g. the (200) reflection in *NaCl* cubic phase split to (200), (020) and (002) in the *Cmcm* orthorhombic phase. From such information the *Cmcm* structure can also be viewed as an orthorhombic distortion of the *NaCl* structure. Two atomic groups of 4(c) sites at the positions (0, y_1, 1/4) and (0, y_2, 1/4) of *Cmcm*, with reflection conditions $h+k = 2n$ in $h\ k\ l$ indices and $h,\ l = 2n$ in $h\ 0\ l$ indices, occupy the same position as the atomic groups of *NaCl* if lattice parameters $a=b=c$, $y_1 = 3/4$ and $y_2 = 1/4$. If $\Delta y = y_1 - y_2 \neq 1/2$, then there are a shearing of alternate (001) planes in the [010] or y direction, can be measured by $2(1 - (y_1+y_2))$ and a zigzag of the [100] atomic rows of *NaCl* structure with $b = b \pm (1/2 - \Delta y)/2$ in the [010] direction as shown in Figure 28.

In Figure 29, The d-spacing are plotted against the pressure. The changes can be observed at 73 and 445 kbar from the disappearance or appearance of the peak(s), or from the change of slope in the d-spacing plot. The lattice parameters at various pressures were refined with the same accuracy and are plotted as a function of pressure as shown in Figure 30. The lattice constants a and c for the chalcopyrite phase, lattice constant a for the cubic phase and the lattice constants a, b and c for the *Cmcm* phase decrease continuously with pressure.

The pressure dependence of the volume is shown in Figure 31. The 1^{st} order phase transition occurs at 70 kbar with a volume reduction of 11.26% and transform completely to the phase II at 87 kbar. The 2^{nd} phase transition starts at 340 - 345 kbar and transformed completely to the phase III - *Cmcm* at 532 kbar.

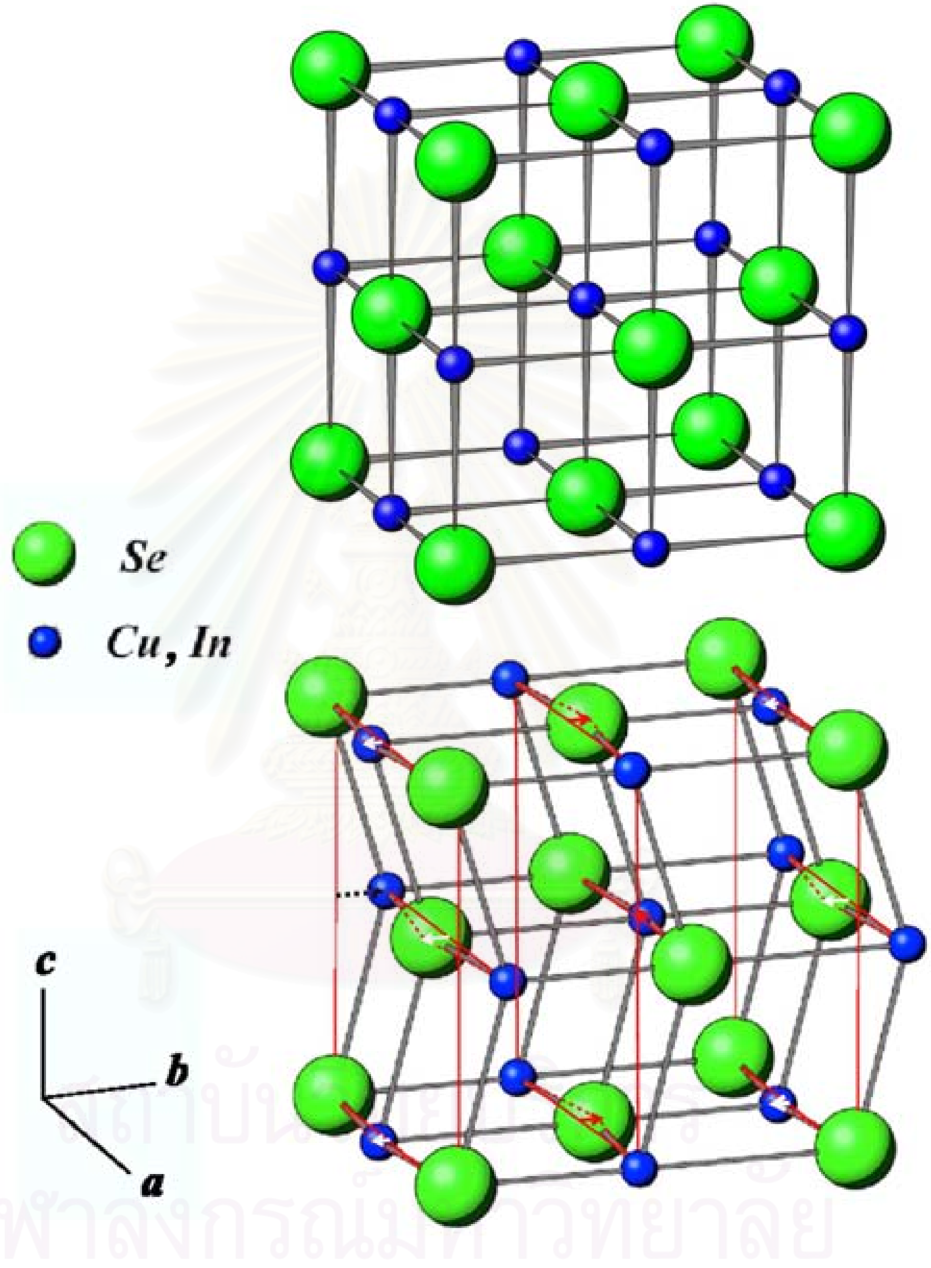

Figure 28: Comparison of the *NaCl* and *Cmcm* structures: upper, *NaCl*; lower, *Cmcm*. If $\Delta y = y_1 - y_2 \neq 1/2$, then there are a shearing of alternate (001) planes in the [010] or y direction, can measure by $2(1 - (y_1 + y_2))$ (black dashed arrow) and a zigzag of the [100] atomic rows of *NaCl* structure with $b = b - (1/2 - \Delta y)/2$ (white arrows), $b + (1/2 - \Delta y)/2$ (red arrows) in the [010] direction.

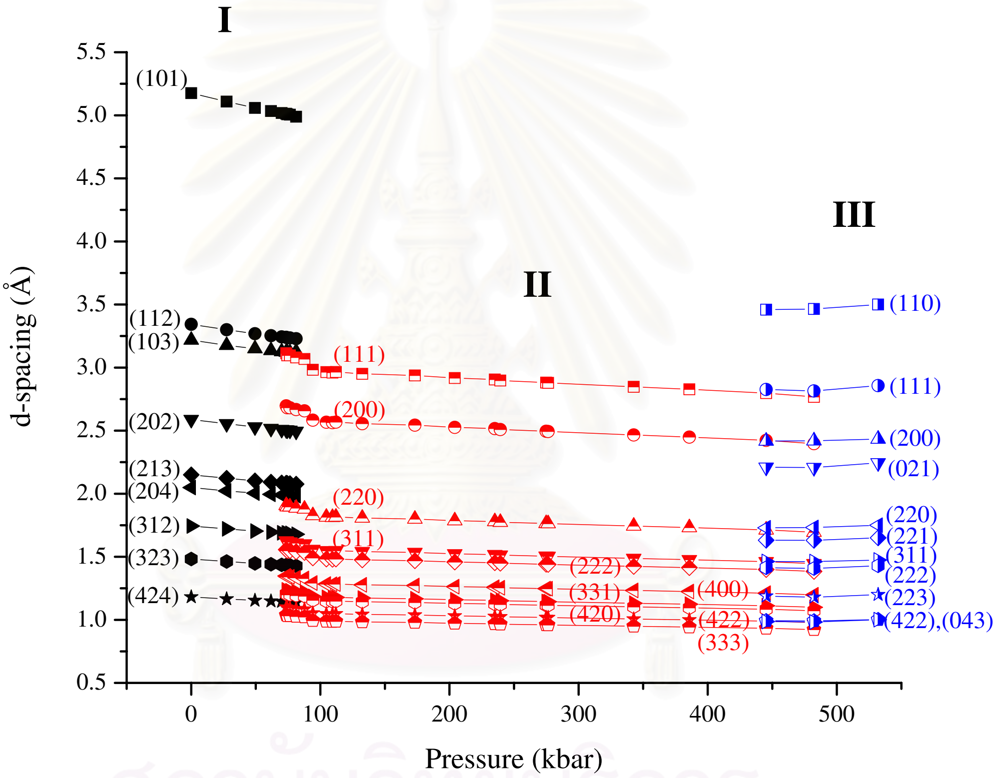

Figure 29: The d-spacing versus pressure for phase I-*chalcopyrite* (black sign), phase II-*cubic* (red sign), and phase III-*Cmcm* (blue sign) of $CuInSe_2$ on pressure increase are shown.

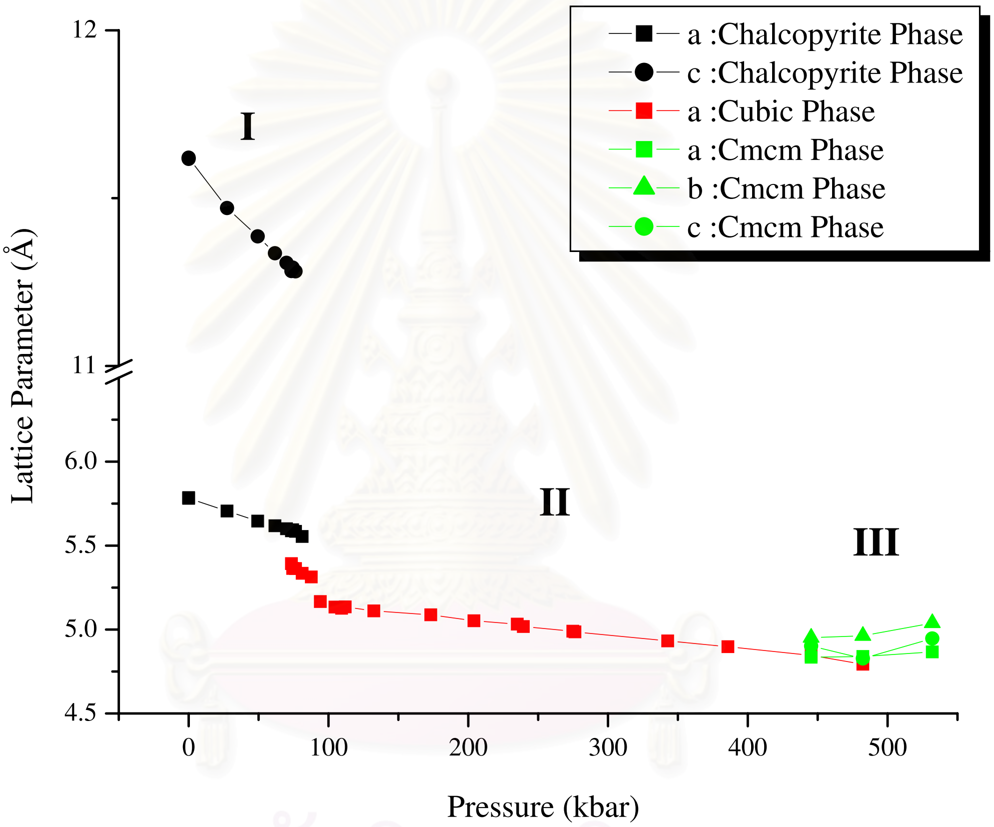

Figure 30: The lattice parameters versus pressure for phase I-*chalcopyrite* (black sign), phase II-*cubic* (red sign), and phase III-*Cmcm* (green sign) of $CuInSe_2$ on pressure increase are shown. The circle signs are represented the lattice parameter a, the triangle signs are represented the lattice parameter b and the square signs are represented the lattice parameter c.

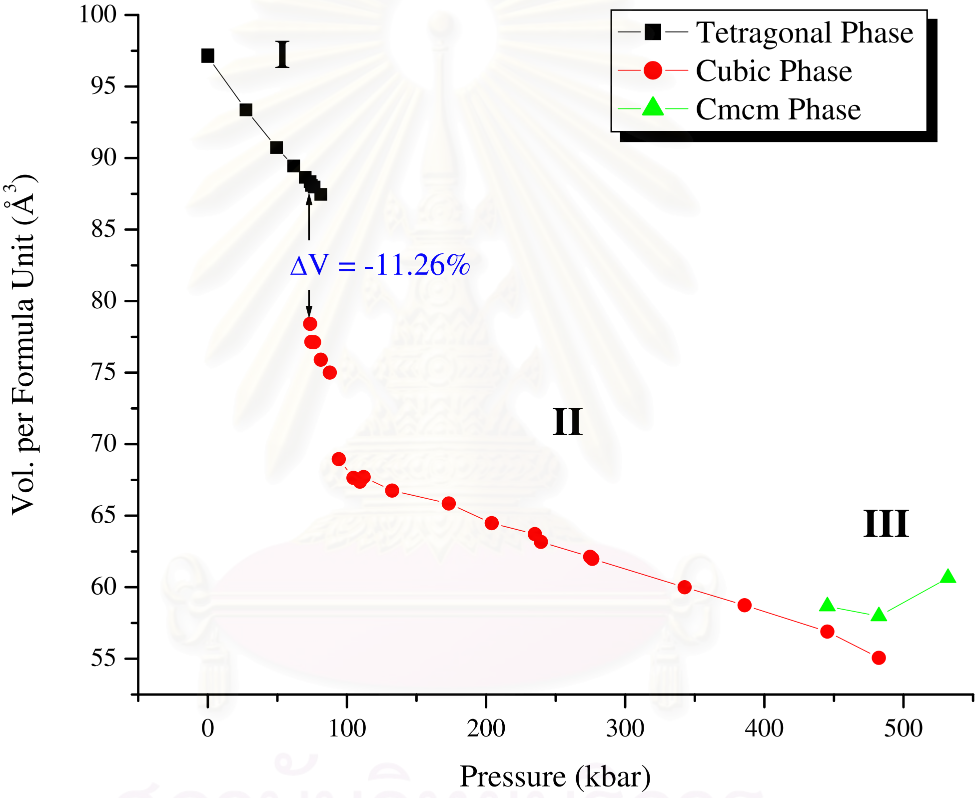

Figure 31: The volume per formula unit versus pressure for phase I-*chalcopyrite* (black sign), phase II-*cubic* (red sign), and phase III-*Cmcm* (green sign) of $CuInSe_2$ on pressure increase are shown, the 1st order phase transition occurs at 70 kbar with a volume reduction of 11.26 %.

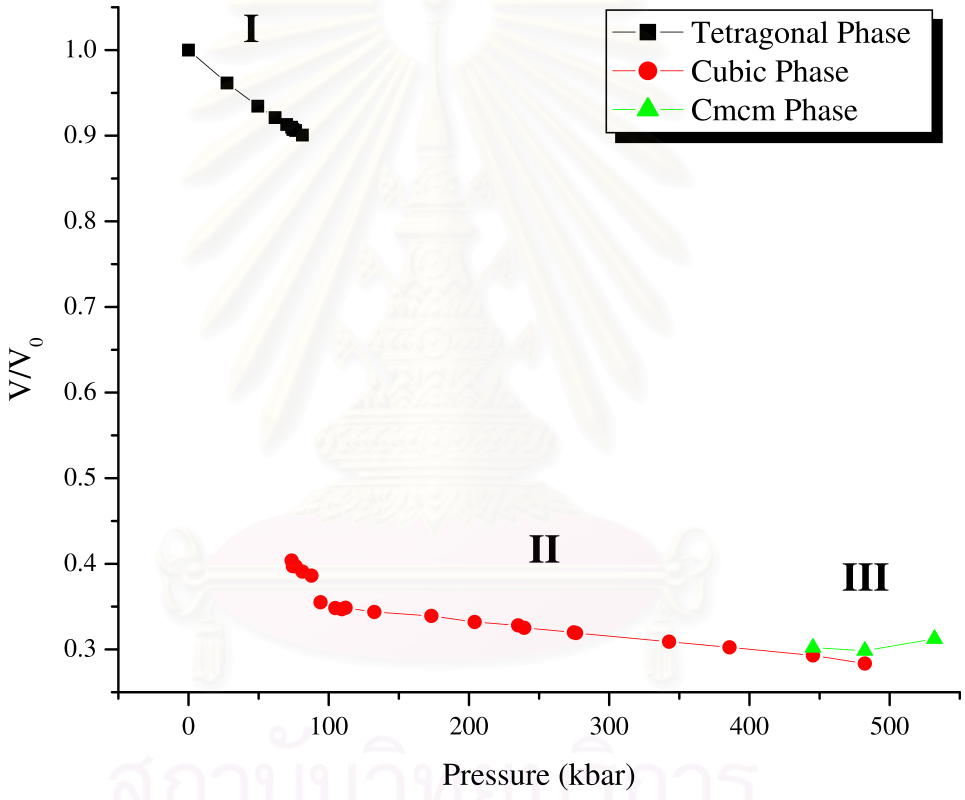

Figure 32: The V/V_0 versus pressure for phase I-*chalcopyrite* (black sign), phase II-*cubic* (red sign), and phase III-*Cmcm* (green sign) of $CuInSe_2$ on pressure increase are shown.

Hydrostatic pressure carries all atoms in the crystal closer together. A smaller atomic separation result in a larger energy gap. Nevertheless, the energy gap in some materials, for example Te and PbSe, diminishes with decreasing interatomic spacing. When the atomic separation decreases, its ionicity becomes greater. The ionicity causes significant changes in the properties of semiconductor. A larger ionicity increases the Coulomb interaction between the ions and also the energy of fundamental gap in the electronic band structure. Whether the ionicity is large enough, the material becomes metal.

The increasing of Coulomb interaction between ions causes the increasing in the cohesive energy of the crystal which favours the high-symmetry structure of increasing coordinate. In the case of $CuInSe_2$, its greater ionicity favours the *Cmcm* structure containing 8-fold coordinated atoms and the rock-salt structure containing 6-fold coordinated atoms rather than tetrahedral bonds in the chalcopyrite structure.

When $CuInSe_2$ in the phase III is quenched, its recovered phase should be the chalcopyrite. Since there are disordered between Cu and In atoms in the phase II, the identification of the atomic positions for Cu and In atoms cannot be recovered when this material reverses to the ambient pressure. So its recovered phase is the zinc-blende structure as shown in Figure 33 and not the chalcopyrite. This assumption agrees with T.Tinoco *et al.*'s report in 1996 [36].

Similar to $CuInSe_2$, Some of the binary semiconductors in III-V and II-VI groups transform from *NaCl* to *Cmcm* structure at high-pressure for example InP, InAs, ZnSe, CdS, CdSe, CdTe, HgSe, and HgTe [7, 37]. Not only these binary semiconductors but the ternary-compound I-III-VI_2, in the same group of $CuInSe_2$, and II-IV-V_2 chalcopyrite structure should also have the same transition sequence. The fact that supports this assumption came from the bonding of these compounds at ambient pressure. Since the bonding of these compounds is tetrahedral, their cohesive energy favour the high-symmetry structure of increasing coordinate to the rock-salt and *Cmcm* structure like those of the binary III-V and II-VI semiconductors and $CuInSe_2$.

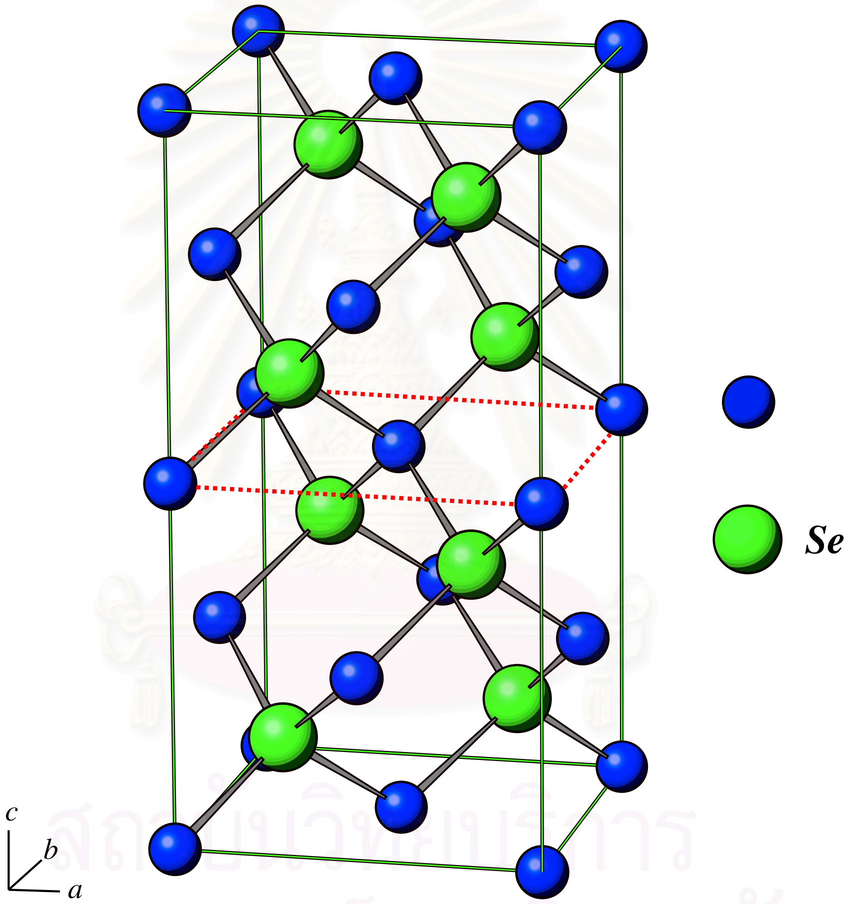

Figure 33: The recovered phase of $CuInSe_2$ is zinc-blende structure.

CHAPTER VI

Conclusions

High pressure x-ray diffraction study for the chalcopyrite semiconductor, $CuInSe_2$, was carried out up to 532 kbar. The Angle Dispersive X-rays Powder Diffraction data were carefully analyzed by the Rietveld refinement.

From the high-pressure x-ray diffraction data of $CuInSe_2$, its crystal structure at ambient pressure is tetragonal chalcopyrite with space group $I\bar{4}2d$ and lattice parameters a = 5.785(5) $\mathring{A}$, c = 11.616(9) $\mathring{A}$ and V = 388.846(1) $\mathring{A}^3$. When the pressure increases, the lattice parameters and volume of unit cell decrease. At 70.03 kbar, the ambient phase start transforming to the 2^{nd} phase. The tetragonal phase is completely transformed to the 2^{nd} phase at 87.73 kbar. The crystal structure of $CuInSe_2$ in the 2^{nd} phase is cubic in space group $Fm\bar{3}m$ or NaCl-like structure with lattice parameters a = 5.315(6) $\mathring{A}$ and V = 75.098 $\mathring{A}^3$. With the increasing pressure, the 2^{nd} phase transition occurs at 339 kbar. The cubic phase is completely transformed to the 3^{rd} phase at 532 kbar. The 3^{rd} phase of $CuInSe_2$ can be indexed as the orthorhombic unit cell with space group $Cmcm$ and lattice parameter a = 4.867(8) $\mathring{A}$, b = 5.023(8) $\mathring{A}$, c = 4.980(3) $\mathring{A}$ and V = 60.8973 $\mathring{A}^3$.

In addition, both the 1^{st} and 2^{nd} phase transition of this material are 1^{st} order phase transition because the pressure dependence of the volume as shown in Figure 31 are slightly changed. The sequence of high pressure crystal structures of $CuInSe_2$ in all phases from 0.001013 to 532 kbar are shown in Figure 34.

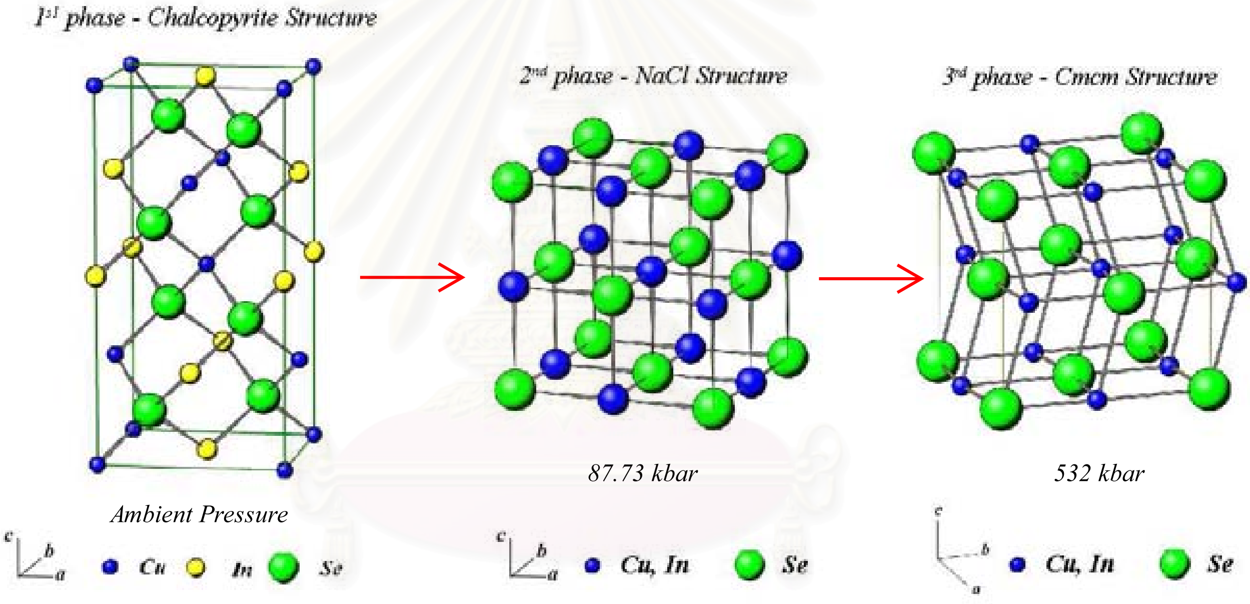

Figure 34: The summarized high pressure crystal structures of $CuInSe_2$ from 0.001013 to 532 kbar.

References

1. J. E. Jaffe and Alex Zunger. Physical Review B **29** (1983): 1882.
2. J. González and C. Rincón. Journal of Applied Physics **65** (1989): 2031.
3. J. González, E. Calclerón, T. Tinoco, J. P. Itié, A. Polian, and E. Moya. J. Phys. Chem. Solids **56** (1995): 507.
4. J. González and C. Rincón. J. Phys. Chem. Solids **51** (1990): 1093.
5. Raymond P. Goehner, Siemens Corporation and Monte C. Michols, Sandia National Laboratories. X-Ray Powder Diffraction, ASM Handbook: Materials Characterization volume 10, The Materials Information Society.
6. O. Shimomura, K. Takemura, H. Fujihisa, Y. Fujii, Y. Ohishi, T. Kikegawa, Y. Amemiya, and T. Matsushita. Review of Scientific Instrument **63** (1992): 967-973.
7. R. J. Nelmes and M. I. McMahon, Structural Transitions in Group IV, III-V, and II-VI Semiconductors under Pressure. Semiconductors and Semimetals **54** (1998): 145.
8. N. G. Wright, R. J. Nelmes, S. A. Belmonte, and M. I. McMahon. J. Synchrotron Radiation **3** (1996): 112.
9. S. A. Belmonte. Ph.D. Thesis. University of Edinburge, (1994).
10. R. J. Nelmes, M. I. McMahon, P. D. Hatton, J. Crain, and R. O. Piltz. Physical Review B **47** (1993): 35.
11. William F. Smith. Foundations of Materials Science and Engineering. 2nd ed. Singapore: McGraw-Hill, 1993.
12. X-ray Diffraction Instruments on GlobalSpec. Available from: http://test-equipment.globalspec.com
13. Bob Baoping He. Powder Diffraction **18** (2003): 71.
14. Thiti Bovornratanaraks. Ph.D. Thesis. The University of Edinburgh, (2001).
15. M. Wunschel. Ph.D. Thesis. Universita Bayneuth, (2003).
16. Shigeru Munekawa and Joseph D. Ferrara. Imaging Plates as Detectors for X-ray Diffraction. Available from: http://www.rigakumsc.com

17. Desgreniers S. and K. Lagarec. Journal of Applied Crystallography **27** (1994): 432.

18. Desgreniers S. and K. Lagarec. Journal of Applied Crystallography **31** (1998): 109.

19. A. Boultif and D. Louer. Journal of Applied Crystallography **24** (1991): 987.

20. T. J. B. Holland and S. A. T. Redfern. Journal of Applied Crystallography **30** (1997): 84.

21. Ali Boultif and Daniel Louër. Journal of Applied Crystallogryphy **37** (2004): 724-731.

22. H. M. Rietveld. Journal Applied Crystallography **2** (1969): 65.

23. R. A. Young. The Rietveld Method. Oxford: University Press, 1993.

24. M. Athee, M. Nurmela, P. Suortii., and M. Jarvinen. Journal of Applied Crystallography **22** (1989): 261.

25. A. C. Larson and R. B. Von Dreele. "General Structure Analyis System (GSAS)" Los Alamos National Laboratory Report LAUR (2000): 86-748.

26. B. H. Toby. Journal of Applied Crystallography **34** (2001): 210-213.

27. High pressure Diamond Optics, Inc.. Available from: http://www.hpdo.com

28. Mohammad Yousuf. Diamond Anvil Cells in High-Presure studies of Semiconductors. Semiconductors and Semimetals **55** (1998): 381.

29. The Diamond-Anvil Cell. Crystallography Laboratory of Virginia Tech. Available from: http://www.crystal.vt.edu

30. L. Merrill and W. A. Bassett. Review of Scientific Instrument **45** (1974): 290.

31. G. J. Piermarini, S. Block, J. D. Barnett, R. A. Forman. Journal of Applied Physics **46** (1975): 2774-2780.

32. D. L. Dekker. Journal of Applied Physics **42** (1971): 3239.

33. H. K. Mao, P. M. Bell, J. W. Shaner, and D. J. Steinberg. Journal of Applied Physics **49** (1978): 3276-3283.

34. Gasper J. Piermarini. Journal of Research of the National Institute of Standards and Technology **106** (2001): 889-920.

35. Synchrotron radiation source. Daresbury Laboratory. United Kingdom. Available: http://www.srs.ac.th

36. T. Tinoco, A. Polian, D. Gomez, and J. P. Itie. Phys. Stat. Sol. (b) **198** (1996): 433.

37. M. I. McMahon and R. J. Nelmes. Phys. Stat. Sol. (b) **198** (1996): 389.

38. High Pressure Physics Group at LLNL-Methods-Synchrotron X-rays, United State of America. Available from: http://www.llnl.gov

39. George H. Stout, Lyle H. Jensen. X-ray Structure Determination. United State of America: The Macmillian Company, 1968.

40. R. J. Nelmes, M. I. McMahon, P. D. Hatton, J. Crain, and R. O. Piltz. Physical Review B **47** (1993): 35-62.

41. Yoshihisa Mori and Kenichi Takarabe. Ternary and Multinary Compounds in the 21^{st} Century IPAP Books 1 (2001): 175-180.

42. A. Mujica, Angel Rubio, A. Muñoz, and R. J. Needs. Reviews of Modern Physics **75** (2003): 863.

43. R. J. Nelmes and M. I. McMahon. Journal of Synchrotron Radiation **1** (1994): 69.

44. Jagan Akella, Bruce Goodwin, and Samuel T. Weir. The Diamond Anvil Cell: Probing the Behavior of Metals under Ultrahigh Pressures. Science and Technology Review March, 1996.

45. B. D. Cullity, S. R. Stock. Elements of X-Ray Diffraction. 3^{rd} ed. New Jersey: Prentice Hall, 2001.

46. Charles Kittel. Introduction to Solid State Physics. 7^{th} ed. United States of America: John Wiley & Sons, 1996.

47. M. I. Eremets. High Pressure Experimental Methods. United States of America: Oxford University Press, 1996.

48. Dennis M. Mills. Third-Generation Hard X-ray Synchrotron Radiation Sources. Canada: John Wiley & Sons, 2002.

49. A. Jayaraman. Reviews of Modern Physics **55** (1983): 65.

50. M. I. McMahon, R. J. Nelmes, D. R. Allan, S. A. Belmonte and T. Bovornratanaraks. Physical Review Letter **80** (1998): 5564-5567.

51. M. I. McMahon, T. Bovornratanaraks, D. R. Allan, S. A. Belmonte and R. J. Nelmes. Physical Review B **61** (2000): 3135-3138.

52. R. J. Nelmes, M. I. McMahon, O. Degtyareva, T. Bovornratanaraks, C. Hejnyl, S. Rekhi, D. R. Allan, J. S. Loveday and S. A. Belmonte. Acta Cryst. **A58** (Supplement) (2002): C178.

53. Jens Als-Nielsen and Des McMorrow. Elements of Modern X-ray Physics. Italy: John Wiley and Sons, 2001.

54. J. Parkes, R. D. Tomlinson and M. J. Hampshire. Journal of Applied Crys tallography **6** (1973): 414.

55. Klaus - Jurgen Range, G. Engert and Armin Weiss. Solid State Communications **7** (1969): 1749-1752.

56. Mitch Miller. Brookhaven National Laboratory. Available from: http://www.bnl.gov

57. Y. Mori, S.-I. Iwamoto, K.-I. Takarabe, S. Minomura, and A. L. Ruoff. Phys. Stat. Sol. (b) **211** (1999): 469.

58. L. C. Ming, T. Eto, K. Takeda, Y. Kobayashi, E. Suzuki, S. Endo, S. K. Sharma, A. Jayaraman, and T. Kikegawa. J. Phys.: Condens. Matter **14** (2002): 10475.

Biography

Varalak Saengsuwan was born in Bangkok, Thailand in 1981. In high school, she studied in Sai Nam Peung School. She did her undergraduate work in physics at Mahidol University, Thailand from 1998 to 2001. Afterward, she worked in the x-rays diffraction group and was awarded a M.Sc. degree in physics from Chulalongkorn University, Thailand in 2004.

Conference Presentations:

1. Varalak Saengsuwan and Thiti Bovornratanaraks. "STRUCTURAL STUDIES OF $CuInSe_2$ UNDER HIGH PRESSURE." *The 29^{th} Congress on Science and Technology of Thailand.* Khon Kaen University, Khon Kaen, Thailand (2003 October 20-22)
2. Varalak Saengsuwan and Thiti Bovornratanaraks. "CRYSTAL STRUCTURE OF $CuInSe_2$ UNDER HIGH PRESSURE." *The 12^{th} Annual Academic Conference.* Chulalongkorn University, Bangkok, Thailand (2004 March 18-19)
3. Varalak Saengsuwan and Thiti Bovornratanaraks. "CRYSTAL STRUCTURE OF $CuInSe_2$ UNDER HIGH PRESSURE." *The 4^{th} National Symposium on Graduate Research.* Graduate School Chiang Mai University, Chiang Mai, Thailand (2004 August 10-11)

Schools:

1. ICTP School on Synchrotron Radiation and Applications - In Memory of J.C. Fuggle and L. Fonda on 19 April - 21 May 2004.